horticulturae

MDPI

Article

Stage-Dependent Callus Induction in *Agapanthus praecox*: Multi-Omics Reveals the Semi-Mature Pedicel Explant as the Optimal Choice

Yan Dong [1], Changmei Du [2], Peiling Li [2], Xingyuan Ye [2], Hui Wang [1] and Jianhua Yue [2,*]

[1] School of Forestry, Xinyang Agriculture and Forestry University, Xinyang 464100, China; dayla2017@163.com (Y.D.)
[2] School of Horticulture, Xinyang Agriculture and Forestry University, Xinyang 464100, China
* Correspondence: jhyues@163.com

Abstract

Callus induction is the foundation for large-scale and rapid plant propagation, and explant age is a key factor affecting callus induction efficiency and in vitro culture outcomes. Pedicels are the main explants for *Agapanthus praecox* tissue culture. This study analyzed three pedicel developmental stages (S1: immature, S2: semi-mature, S3: mature) and their induced calli (C1, C2, C3). We integrated transcriptomics, metabolomics (LC-MS/GC-MS), quantitative real-time PCR (qRT-PCR), and weighted gene co-expression network analysis (WGCNA) to clarify the physiological and molecular mechanisms of pedicel regenerative potential. Results showed that S2 exhibited the highest callus induction rate, while C2 showed superior proliferation coefficients and regenerative potential. In pedicel samples, differentially expressed genes were significantly enriched in the MAPK signaling pathway and plant hormone signal transduction pathway, while differentially accumulated metabolites were linked to energy metabolism, amino acid/nucleotide metabolism, and stress responses. Key metabolites (e.g., carbohydrates, amino acids, thidiazuron, and *β*-chlorogenin) played specific roles in maintaining the meristematic capacity of pedicels. qRT-PCR further confirmed that S2 maintained balanced endogenous hormone signaling and proper cell wall modification. Furthermore, WGCNA identified a key module associated with oxidative stress responses along with S2. Overall, the regenerative potential of pedicel is mediated by the balanced hormone signal transduction, metabolic reprogramming, and epigenetic regulation in *A. praecox*.

Keywords: *Agapanthus praecox*; explant; developmental stage; cell reprogramming; plant hormone signal transduction; regenerative capacity

Check for updates

Academic Editor: Othmane Merah

Received: 3 December 2025
Revised: 22 December 2025
Accepted: 25 December 2025
Published: 26 December 2025

Copyright: © 2025 by the authors. Licensee MDPI, Basel, Switzerland. This article is an open access article distributed under the terms and conditions of the Creative Commons Attribution (CC BY) license.

1. Introduction

Plants can regenerate via callus, which is key for large-scale, rapid in vitro propagation. Unlike direct regeneration, indirect (callus-mediated) regeneration has an intermediate stage where cells first dedifferentiate, proliferate, and then redifferentiate to form various plant organs and tissues [1,2]. In this context, the explant serves as the crucial factor determining the effectiveness of induction and the regenerative potential [3]. As the initial material, the explant possesses a variety of inherent characteristics [4].

Explants from different plant organs vary significantly in callus induction ability [1,2,4–8]. Meristematic tissues (e.g., shoot tips, root tips) typically have robust cell division activity,

high callus induction potential [9], vigorous metabolism, short cell cycles, and high endogenous auxin/cytokinin (CTK) levels, which are key factors for initiating cell dedifferentiation [10]. Nodal and stem segment explants have unique induction advantages: possessing meristematic potential, maintaining a stable nutritional and hormonal microenvironment, and for some, rapidly producing high-quality, vigorous callus [4]. In practice, the nodal explants of *Lycium barbarum* L. show a higher induction success rate than hypocotyls [4], while petiole explants yield the best callus induction in *Papaver rhoeas* L. [1]. Hypocotyls with cotyledonary nodes and shoot apical meristems show significantly higher regenerative potential than those without these structures in *Cannabis sativa* L. [11]. Leaves are primary photosynthetic organs and common explants [2,12], but their callus induction ability varies greatly across species. For instance, the leaves of herbaceous plants are relatively easy to induce [13,14], whereas callus formation from some woody plants is more difficult [15]. In *Centratherum punctatum* Cass., petiolate leaves have stronger regenerative potential than petiole-less ones [2]. In *Carica papaya* L. [16] and *Fragaria* spp. [7], leaf-derived explants root more readily than stem-derived ones. However, most monocot leaf cells are highly differentiated, making callus-related dedifferentiation challenging [17]. Notably, dormant buds are ideal for embryogenic callus (EC) induction in *Schisandra chinensis* (Turcz.) Baill [18] and *Paeonia suffruticosa* [8], while male flower buds are optimal for the large-scale commercial propagation of *Musa* spp. variety Udhayam [5]. Collectively, meristem-rich organs (e.g., shoot tips, nodes) or photosynthetically active tissues (e.g., petiolate leaves) are generally more suitable for callus induction.

Within the same organ, the explant position also influences induction efficiency [10]. In *Toona sinensis*, basal leaf and hypocotyl sections show higher callus induction [12]. Leaves with midrib vascular bundle cells were proven to be excellent explants in *Garcinia* species [19]. Histological and transcriptomic analyses combined with in vitro induction assays demonstrated that EC arises from the adaxial side and non-EC from the abaxial side of *Cucumis sativus* L. cotyledon nodes, and that indole-3-acetic acid (IAA) and CTK are key mediators of the cellular dedifferentiation and redifferentiation regulating this differential callus development [10]. These patterns reflect underlying differences in cellular differentiation and meristematic activity.

The explant developmental stage profoundly affects callus induction, with a well-documented trend: young explants are more likely to be induced to form callus than mature explants [2,7,12,20]. This is attributed to young cells' low differentiation level, thin cell walls, high metabolic activity, and strong hormone sensitivity, and these traits facilitate cell dedifferentiation, a key step in callus induction [10]. The callus induction and shoot regeneration capacity of cotyledonary leaf segments were found significantly related to the age of the explants, and the youngest explants induced the highest regeneration response in *Jatropha curcas* L. [20]. Conversely, middle-aged leaves and hypocotyls exhibit better callus induction rates than young explants in *Toona sinensis* [12].

Callus induction efficiency differs by explant type, location, and age, mainly due to variations in their physiological characteristics: endogenous hormone levels, nutrient content, and cell activity [21]. Species-specific endogenous hormone levels drive distinct callus induction and proliferation across plant species [22,23]. Among endogenous hormones, IAA, CTK, and gibberellin (GA) are critical for plant cell growth, differentiation, and dedifferentiation [2,6,21,24]. Elevated IAA, CTK, and GA levels enhance cell division and dedifferentiation, thus promoting callus formation [25]. For certain plants, explants with high endogenous IAA and CTK levels during vigorous growth stages exhibit higher callus induction rates [17]. A cultivar showing the highest regeneration ability in *Hordeum vulgare* had the highest levels of IAA and zeatin [21]. *Auxin response factor 4* (*ARF4*), which acts upstream of *lateral organ boundaries domain 16*, promotes adventitious root formation in

Prunus persica, a mechanism consistent with IAA's role in callus induction [26]. Integrated transcriptomic and proteomic analyses of immature (high embryogenic potential) and mature (low embryogenic potential) zygotic embryos of maize during callus induction revealed that high-embryogenic explants and their derived callus are enriched in cell proliferation and plant hormone signal transduction pathways [27].

Explant nutrient content (carbohydrates, nitrogen, and phosphorus sources) is another key factor: carbohydrates (starch, soluble sugars) supply energy and carbon skeletons for induction [28]; appropriate nitrate/ammonium nitrogen levels favor callus formation [25]; and phosphorus supports cell division and growth [29,30]. Explant cell activity is also directly linked to induction. Explants with high activity have a vigorous metabolism and strong hormone and nutrient responses, aiding induction [31].

Beyond intrinsic traits, external conditions, especially plant growth regulator (PGR) combinations, strongly impact callus induction and secondary metabolite accumulation [4,32]. For example, CTK/auxin combinations enhance chlorogenic/caffeic acid accumulation and alter callus phenolic profiles in *Lycium barbarum* [4] by modifying the explants' endogenous hormone balance [33]. Moreover, auxin acts as a key driver of epigenetic modifications that govern callus formation: high auxin levels induce callus development in *Arabidopsis* through methyltransferase-mediated histone H3K36 methylation [6], while DNA methylation also modulates callus formation in strawberry leaf explants [34].

Agapanthus praecox, a perennial herbaceous plant native to South Africa [35], is prized for its medicinal properties, with recent research focusing on its chemical composition and pharmacological potential [36,37]. It contains bioactive compounds such as saponins (anti-inflammatory, antimicrobial, and antitumor), flavonoids (antioxidant, anti-inflammatory, and anticancer), alkaloids (potential neurological effects), and polysaccharides (immune-enhancing and antitumor) [36–38]. However, the low efficiency of traditional propagation methods (e.g., division) and the lack of optimized tissue culture protocols have restricted the large-scale production of *A. praecox*.

The tissue culture of *A. praecox* is of significant importance in rapid propagation, variety improvement, germplasm preservation, medicinal component production, and extraction. It serves as a key technology for promoting its industrialization and sustainable development [39]. In previous studies on *A. praecox*, flower buds have predominantly been utilized as explants; however, systematic investigations into the optimal maturation stage of these buds and their underlying regulatory mechanisms remain scarce. Additionally, the influence of explant developmental stage on callus induction efficiency is poorly understood [27].

To address these challenges, this study systematically analyzed the morphological and physiological characteristics of pedicel explants and correlated these traits with callus induction efficiency. Meanwhile, using transcriptome sequencing and non-targeted metabolomics, the study explored in depth the molecular and physiological mechanisms underlying explant-mediated callus induction. This comprehensive research approach aims to lay a solid foundation for optimizing the tissue culture of *A. praecox*. Its specific objectives include identifying stage-specific markers (e.g., metabolic or transcriptional) applicable to explant selection and clarifying the regulatory mechanisms of the dedifferentiation process.

2. Materials and Methods

2.1. Plant Materials and Growth Conditions

Four-year-old plants of *A. praecox* were grown in the greenhouse of Xinyang Agriculture and Forestry University, Xinyang, China (32°9′ N, 114°7′ E), under natural light conditions with indoor temperatures of approximately 20–25 °C (night) and 25–35 °C (day), a 14 h photoperiod, and 60–70% relative humidity. The plants were grown in pots (30 cm

in diameter and 35 cm deep) filled with a mixture of vermiculite/peat (1:1, v/v). All the plants were subjected to routine management.

In May 2022, different developmental stages of flower buds (S1: stage 1, immature; S2: stage 2, semi-mature; S3: stage 3, mature) were excised from adult plants and washed with running water for 30 min. Then, they were rinsed with distilled water three times. Subsequently, the flower buds were disinfected with 75% (v/v) ethanol for 60 s and 2% (v/v) sodium hypochlorite for 10 min. Finally, the explants were rinsed with sterile, distilled water three times. A total number of 31 (S1), 22 (S2), and 28 (S3) flower buds were used for callus induction, and the explants obtained from each bud were inoculated in one Petri dish. For callus induction, the pedicels of disinfected buds were separated and cut into 5 mm long segments and used as initial explants. Simultaneously, pedicels (S1, S2, and S3) were sampled from flower buds, frozen in liquid nitrogen, and stored at −80 °C for high-throughput omics analysis (transcriptome and metabolome).

The callus was induced using MS [40] medium (PhytoTechnology Laboratories, Shawnee Mission, KS, USA) containing 8.28 μM picloram (PIC; BBI, Sangon Biotech, Shanghai, China) and 87.6 mM sucrose (BBI, Sangon Biotech, Shanghai, China), with 20–25 pedicel segments inoculated per Petri dish (90 mm in diameter). Calli were named C1, C2, and C3 corresponding to explants S1, S2, and S3, respectively. The callus induction rate was calculated after one month. Incubation was carried out in a phytotron in the dark at 25 ± 1 °C. After two subculture cycles (60 d), the calli were sampled for subsequent experiments.

2.2. Morphological and Microscopic Observation

The fresh samples of pedicel and scape (main floral stem) were fixed immediately in formalin/acetic acid/70% ethanol (FAA, 5/5/90, $v/v/v$), dehydrated in an ascending ethanol series, immersed with xylene, and embedded in paraffin. All operations involving xylene and acetic acid were performed in a laboratory fume hood. Sections were cut to a thickness of 8–10 μm using a rotary microtome (Leica RM2235, Wetzlar, Germany). Slides were stained with safranin O (BBI, Sangon Biotech, Shanghai, China) and hematoxylin (BBI, Sangon Biotech, Shanghai, China) for cell size observation and with periodic acid-Schiff (PAS) for polysaccharide identification. The morphological images of the pedicel were captured using Axio Scope A1 microscope (Carl Zeiss, Oberkochen, Germany).

For microscopic cell observation, fresh callus (<5 mm^3) was immediately transferred to a 1.5 mL Eppendorf tube, and the samples were suspended in 0.5 mL of 1% (w/v) acetocarmine for 30 min. Next, the callus suspensions were diluted with double-distilled water (ddH_2O), the suspension, including callus cells, was transferred to a slide using a pipette, and a cover glass was slightly placed on the slide. Microscopic observations were performed using an Axio Scope A1 microscope (Carl Zeiss, Oberkochen, Germany).

2.3. Callus Multiplication

Approximately one gram of callus was accurately weighed on a clean bench, after which the cell mass was equally divided into nine smaller cell masses. One biological replicate consisted of five Petri dishes, with three independent biological replicates performed. Callus samples were sub-cultured monthly onto fresh MS medium containing 6.21 μM PIC and 87.6 mM sucrose, and incubation was performed as above. The weight of the callus in each Petri dish was measured with an accuracy of 0.01 g. All weighing data were recorded for calculating the callus multiplication coefficient. Multiplication coefficient = weight after subculture proliferation/initial weight of callus.

2.4. Transcriptomic Sequencing and Analysis

For transcriptomic analysis, a total of 18 samples were used, including three biological replicates for each of the six sample types (S1, S2, and S3; C1, C2, and C3). Total RNA was extracted from each sample using the RNAiso Plus kit (TaKaRa, Dalian, China) following the manufacturer's protocol. To avoid genomic DNA contamination, 1.0 μL of RNase-free DNase I (TaKaRa, Dalian, China) was added to each RNA sample and incubated at 37 °C for 30 min. RNA quality and integrity were evaluated by electrophoresis on 1% agarose gel and spectrophotometry with a NanoDropTM 2000 Spectrophotometer (Thermo Fisher Scientific, Waltham, MA, USA). Transcriptome sequencing and subsequent bioinformatics analysis were performed by OE Biotech Co., Ltd. (Shanghai, China; https://www.oebiotech.com/, accessed on 15 December 2025). After library construction (Illumina, San Diego, CA, USA) carried out according to Illumina standard instructions), the libraries were sequenced on an Illumina HiSeq 2500 platform with a paired-end 150 bp sequencing mode. Raw reads were subjected to quality control (QC), followed by filtering to remove adapter-containing reads and low-quality reads. The Illumina RNA-Seq adapters were searched and removed by Cutadapt 3.5 using default parameters. Since no reference genome of *A. praecox* is currently available, the de novo assembly of clean reads was performed using Trinity v2.15.1 with default parameters. The assembled transcripts were clustered using Corset to remove redundancy and obtain unigenes. Fragments per kilobase per million (FPKM) mapped reads values were calculated by Ballgown. Differential expression analyses were performed by comparing gene expression levels between different sample groups, and differentially expressed genes (DEGs) were selected based on a false discovery rate (FDR) of 0.05. The FPKM method was used to calculate the expression levels of the identified genes. Genes with a fold change (FC) >2 and adjusted *p*-value (P_{adj}) < 0.05 were considered as DEGs and were mapped to terms in the Gene Ontology (GO) database (http://www.geneontology.org/, accessed on 15 December 2025), where gene numbers for each term were calculated to identify significantly enriched GO terms based on a hypergeometric test. In addition, pathway enrichment analysis was conducted utilizing the Kyoto Encyclopedia of Genes and Genomes (KEGG, http://www.kegg.jp/, accessed on 15 December 2025).

2.5. Sample Processing for Metabolite Extraction

Dual-platform metabolomics including liquid chromatography-mass spectrometry (LC-MS) and gas chromatography-mass spectrometry (GC-MS) was performed in this study.

For the LC-MS and GC-MS test, 60 mg of each sample (S1, S2, S3, C1, C2, C3; three biological replicates per group) were transferred to a 1.5 mL Eppendorf tube, respectively. Two small steel balls were added to each tube, followed by 4 μg·mL^{-1} L-2-chlorophenylalanine dissolved in methanol as internal standard, and 600 μL of methanol/water (7:3 for LC-MS and 1:1 for GC-MS, *v*/*v*). Samples were placed at −80 °C for 2 min, ground at 60 Hz for 2 min, subjected to ultrasonic extraction for 30 min in an ice-water bath, and then placed at −40 °C overnight.

After this time, samples were centrifuged at 4 °C (12,000 rpm) for 10 min; after which 150 μL of supernatant from each tube was collected using a glass syringe, filtered through a 0.22 μm microfilters and transferred to LC vials. The vials were stored at −80 °C until LC-MS analysis.

The resulting mixture was vortexed vigorously for 2 min and incubated at 37 °C for 60 min. Fifty microliters of BSTFA (with 1% TMCS) and 20 μL n-hexane were added into the mixture, which was vortexed vigorously for 2 min and then derivatized at 70 °C for 60 min. The samples were placed at ambient temperature for 30 min before GC-MS analysis.

QC samples were prepared by mixing 10 μL of supernatant from each sample (n = 18) to monitor instrument stability during the entire analysis. QC samples underwent the same subsequent processing (drying, derivatization) as experimental samples to monitor instrument stability for GC-MS analysis.

2.6. LC-MS Metabolomic Analysis

Metabolic profiling was analyzed using a Waters ACQUITY UPLC I-Class system (Waters Corporation, Milford, CT, USA) coupled with a Waters VION IMS Qtof Mass Spectrometer (Waters Corporation, Milford, CT, USA) in both electrospray ionization positive (ESI+) and negative (ESI−) modes. Samples were analyzed in two batches (one for ESI+ and one for ESI−) to avoid mode-switching interference. An ACQUITY UPLC BEH C18 column (1.8 μm particle size, 2.1 mm × 100 mm; Waters Corporation) was used for both ion modes. Water and acetonitrile/methanol (2:3, v/v), both containing 0.1% formic acid were used as mobile phases A and B, respectively. The flow rate was 0.35 mL·min^{-1} and the column temperature was 45 °C. All the samples were kept at 4 °C during the analysis. The injection volume was 5.0 μL.

Data acquisition was performed in full-scan mode (m/z range: 50–1000) combined with MSE mode (Waters' proprietary data-independent acquisition mode), which alternates two independent scans with different collision energies (CE) during each run. Parameters of mass spectrometry were as follows: a low-energy scan (CE 4 eV), and a high-energy scan (CE ramp 20–45 eV) to fragment the ions. Argon (99.999%) was used as collision-induced dissociation gas; scan time: 0.2 s; interscan delay: 0.02 s; capillary voltage: 2.5 kV; cone voltage: 40 V; source temperature: 115 °C; desolvation gas temperature: 450 °C; desolvation gas flow, 900 L·h^{-1}.

2.7. GC-MS Metabolomic Analysis

Then, 80 μL of 15 mg·mL^{-1} methoxylamine hydrochloride in pyridine was subsequently added. The resultant mixture was vortexed vigorously for 2 min and incubated at 37 °C for 60 min. Moreover, 50 μL of BSTFA (with 1% TMCS) and 20 μL n-hexane were added into the mixture, which was vortexed vigorously for 2 min and then derivatized at 70 °C for 60 min. The samples were placed at ambient temperature for 30 min before GC-MS analysis.

Derivatized samples were analyzed using an Agilent 7890B GC system coupled to an Agilent 5977A Mass Spectrometry Detector (Agilent Technologies Inc., Santa Clara, CA, USA). A DB-5MS fused-silica capillary column (30 m × 0.25 mm × 0.25 μm, Agilent J & W Scientific, CA, USA) was used to separate the derivatives. Helium (>99.999%) was used as the carrier gas at a constant flow rate of 1 mL·min^{-1} through the column. The injector temperature was maintained at 260 °C. The injection volume was 1.0 μL in the split-less mode. The initial oven temperature was 60 °C, ramped to 125 °C at a rate of 8 °C·min^{-1}, to 210 °C at a rate of 4 °C·min^{-1}, to 270 °C at a rate of 5 °C·min^{-1}, to 305 °C at a rate of 10 °C·min^{-1}, and finally held at 305 °C for 3 min. The temperature of MS quadrupole and ion source (electron impact) was set to 150 °C, and 230 °C, respectively. The collision energy was 70 eV. The mass data were acquired in a full-scan mode (m/z range 50 to 500).

2.8. Metabolomic Data Preprocessing and Statistical Analysis

Metabolomic data preprocessing was performed using two software tools, corresponding to LC-MS and GC-MS data, respectively. LC-MS data was processed with Progenesis QI software (v2.3, Waters Corporation, Milford, CT, USA); and GC-MS data was processed with Agilent MassHunter Qualitative Analysis B.07.00 software (Agilent Technologies, Santa Clara, CA, USA) for raw peak extraction, followed by MetaboAnalyst 5.0 (https://www.metaboanalyst.ca/, accessed on 15 December 2025) for further

preprocessing. Metabolites were annotated based on the Fiehn and NIST databases. After alignment using statistical alignment component, the raw data array was obtained from the preprocessed raw peak data as a three-dimensional dataset (including sample information, peak names, and peak intensities). After peaks with RSD of the internal standard > 0.3 were deleted, all peak intensities (peak areas) were processed by normalization using multi-internal standards according to retention time partition period. Data were transformed by $\log_{10}$, and the generated data matrix was imported into the SIMCA 14.0 software package (Umetrics, Umeå, Sweden). PCA and (orthogonal) partial least-squares-discriminant analysis [(O)PLS-DA] were performed to visualize the metabolic difference among experimental groups after mean centering and unit variance scaling. Variables with a Variable Importance in Projection (VIP) $\geq$ 1.0 (from OPLS-DA model) were considered more relevant for group discrimination. Metabolites meeting VIP $\geq$ 1.0 and $P_{adj} \leq 0.05$ were defined as significant differentially accumulated metabolites (DAMs). KEGG pathway analysis of metabolites was performed using the R package "clusterProfiler" (v4.6.0) by Luming Biotechnology Co., Ltd. (Shanghai, China).

2.9. Integrated Transcriptomic and Metabolomic Analysis

Integrated transcriptomic and metabolomic analysis was performed to explore the regulatory relationships between DEGs and DAMs. For functionally associated DEG-DAM pairs, the $\log_2$-FC values of DEGs and $\log_2$-FC values of DAMs (the same comparison group) were used to evaluate expression consistency. Based on the $\log_2$-FC of DEGs and DAMs, the Spearman correlation coefficients and associated p values were calculated; the correlation plots of comparative analyses were also drawn. The results of KEGG pathway enrichment analyses were then visualized. Moreover, the functionally associated DEG-DAM pairs were mapped to the reference pathways in the KEGG database to better understand the regulatory status of DEGs and DAMs in pathways. KEGG pathways with corrected $p < 0.05$ were considered significantly enriched, and TBtools (v1.1.20) was used to generate heat maps [41].

2.10. Weighted Gene Co-Expression Network Analysis (WGCNA)

WGCNA was performed using the WGCNA package in R (v3.6.1) to identify gene co-expression modules associated with callus induction capacity and key transcription factors (TFs) regulating these modules [42]. Prior to network construction, the gene expression matrix was preprocessed by filtering out low-expression genes, followed by variance-stabilizing transformation and quantile normalization. A soft-thresholding power (β) was determined using the pickSoftThreshold function to approximate a scale-free topology. Adjacency matrices were computed based on Pearson correlation coefficients between gene expression profiles, and topological overlap matrices (TOMs) were derived to measure network connectivity. Genes were then hierarchically clustered using TOM-based dissimilarity, and modules were detected using the dynamic tree cut algorithm with a minimum module size of 30. Modules with high eigengene correlation (e.g., correlation > 0.85) were merged. For each co-expression module, the module eigengene was computed. The correlation between each module eigengene and sample traits (or group information) was analyzed using *Pearson* correlation, with significance assessed via permutation tests. Module membership and gene significance were calculated to identify hub genes. The co-expression network was visualized in Cytoscape (v3.10.1) using the cytoHubba plugin, with edges weighted by TOM values and nodes filtered based on module membership and connectivity.

2.11. Quantitative Real-Time PCR (qRT-PCR)

One microgram of total RNA was used for reverse transcription using the PrimeScript™ 1st Strand cDNA Synthesis Kit (TaKaRa, Dalian, China). Based on the RNA-Seq results, the key DEGs identified in the transcriptome analysis were further quantitatively validated by qRT-PCR technology using an ABI 7500 Fast PCR Detection System (Life Technologies) according to the manufacturer's instructions. The expression values obtained were normalized against β-actin. All primer sequences are presented in Supplementary Table S1. The primers were adopted from our prior work in *A. praecox* [43]. Primer efficiency was systematically validated via the standard curve method prior to qRT-PCR. The relative gene expression levels were analyzed according to the $2^{-\Delta\Delta Ct}$ method [44]. The heatmap integrating FC and *p* values was generated using Metware Cloud, a free online platform for data analysis (https://cloud.metware.cn, accessed on 15 December 2025).

2.12. Statistical Analysis

The data, including callus induction rate and multiplication coefficients, are presented as mean ± standard error (SE) from three independent replicates. The data were statistically analyzed using one-way analysis of variance (ANOVA) with SPSS software (v20.0, SPSS Inc., Chicago, IL, USA). Homogeneity of variance was tested prior to ANOVA. The significance of differences among means was determined by post hoc Duncan's multiple range test at a significance level of $p < 0.05$.

3. Results

3.1. Morphological, Histological, and Regeneration Potential of Pedicels

Pedicel explants exhibited considerable morphological variation across developmental stages (S1–S3; Figure 1A). Induced callus originated from vascular parenchyma cells, and the callus was typically translucent and watery; C3 was smaller than C1 and C2 (Figure 1B). Cellular morphology, visualized by acetocarmine staining, revealed distinct features: C1 cells showed a prolate-elliptical shape, with thin cytoplasm and faintly stained cell nuclei; C2 cells were spherical with dense cytoplasm and intensely stained cell nuclei, and C3 cells were spherical with thin cytoplasm (Figure 1C). Histological observations of transverse and longitudinal sections of the pedicels showed a clear developmental trend: Parenchymal cells (Pcs) gradually increased in size with vascular bundles (Vbs) becoming progressively more dispersed from S1 to S3 (Figure 1D). Callus induction rates showed significant differences among pedicel stages; despite being more tender, S1 exhibited a significantly lower induction rate than S2 and S3 ($p < 0.05$; Figure 1E). Significant differences were also observed in callus proliferation efficiency, with C2 displaying the highest multiplication coefficient and C1 the lowest (Figure 1F). Notably, while cell sizes at the scape apex were relatively uniform, longitudinal axis lengths differed among scapes; and in both cross and longitudinal sections, cells of pedicels continuously increased in size as they developed and matured (Figure 1G). Furthermore, we found that with the maturation of pedicels, the accumulation of starch granules decreased progressively in both scapes and pedicels (Figure 1H).

3.2. Transcriptomic Analyses of Pedicels and Pedicel-Derived Calli

Quantitative analysis showed distinct DEG counts across comparison groups (Figure 2A). For pedicel samples, the number of DEGs identified in intra-group comparisons varied with developmental stage: 2668 DEGs were detected between S1 and S2, while a substantially higher number (10,405) were observed in S1/S3. Similarly, in the callus group, 6674 DEGs were found in C1/C2, whereas C1/C3 exhibited the highest number of DEGs (11,372) among all callus comparisons (Figure 2A). Furthermore, PCA

revealed differences among pedicel and callus samples. Notably, groups were separated well along PC1 (30.56% variance) and PC2 (11.94% variance) (Figure 2B).

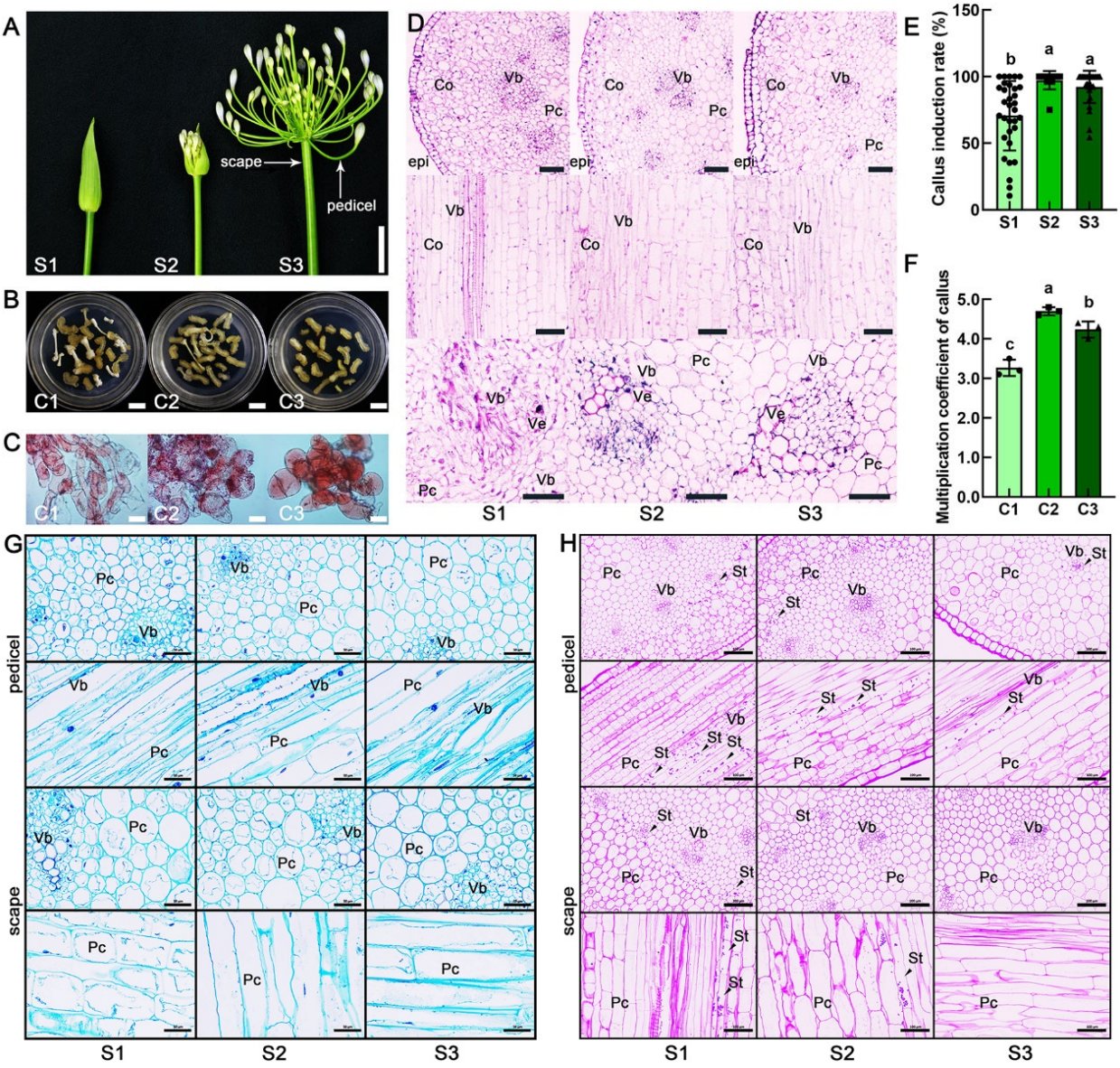


Figure 1. Morphological differences and regeneration potential of pedicels and pedicel-derived calli. (**A**) Morphology of pedicels of S1, S2, and S3, corresponding to flower bud stages 1, 2, and 3, respectively. Scale bar = 3.0 cm. (**B**) Morphology of callus samples C1, C2, and C3, derived from S1, S2, and S3, respectively. Scale bar = 1.0 cm. (**C**) Cellular morphology of callus samples C1, C2, and C3. Scale bar = 100 μm. (**D**) Microscopic observations of pedicel samples S1, S2, and S3, showing transverse and longitudinal sections. Scale bars = 200 μm. Abbreviations: epi, epidermis; Co, cortex; Vb, vascular bundle; Ve, vessel; Pc, parenchymal cell. (**E**) Callus induction rate. Data are presented as mean ± SE; $n = 31$ (S1), $n = 22$ (S2), and $n = 28$ (S3). Means marked by the same letter on the bar are not significantly different according to Duncan's multiple range test at $p < 0.05$, and the same hereinafter. (**F**) Callus multiplication coefficient. Data are presented as mean ± SE; $n = 3$. (**G**) Morphological differences in samples from pedicel and scape by hematoxylin staining. The micromorphology of transverse and longitudinal sections were provided. Scale bars = 50 μm; Vb: vascular bundle; Pc: parenchymal cell. (**H**) PAS staining of pedicel and scape. Scale bars = 100 μm; Vb: vascular bundle; Pc: parenchymal cell; St: starch granule.

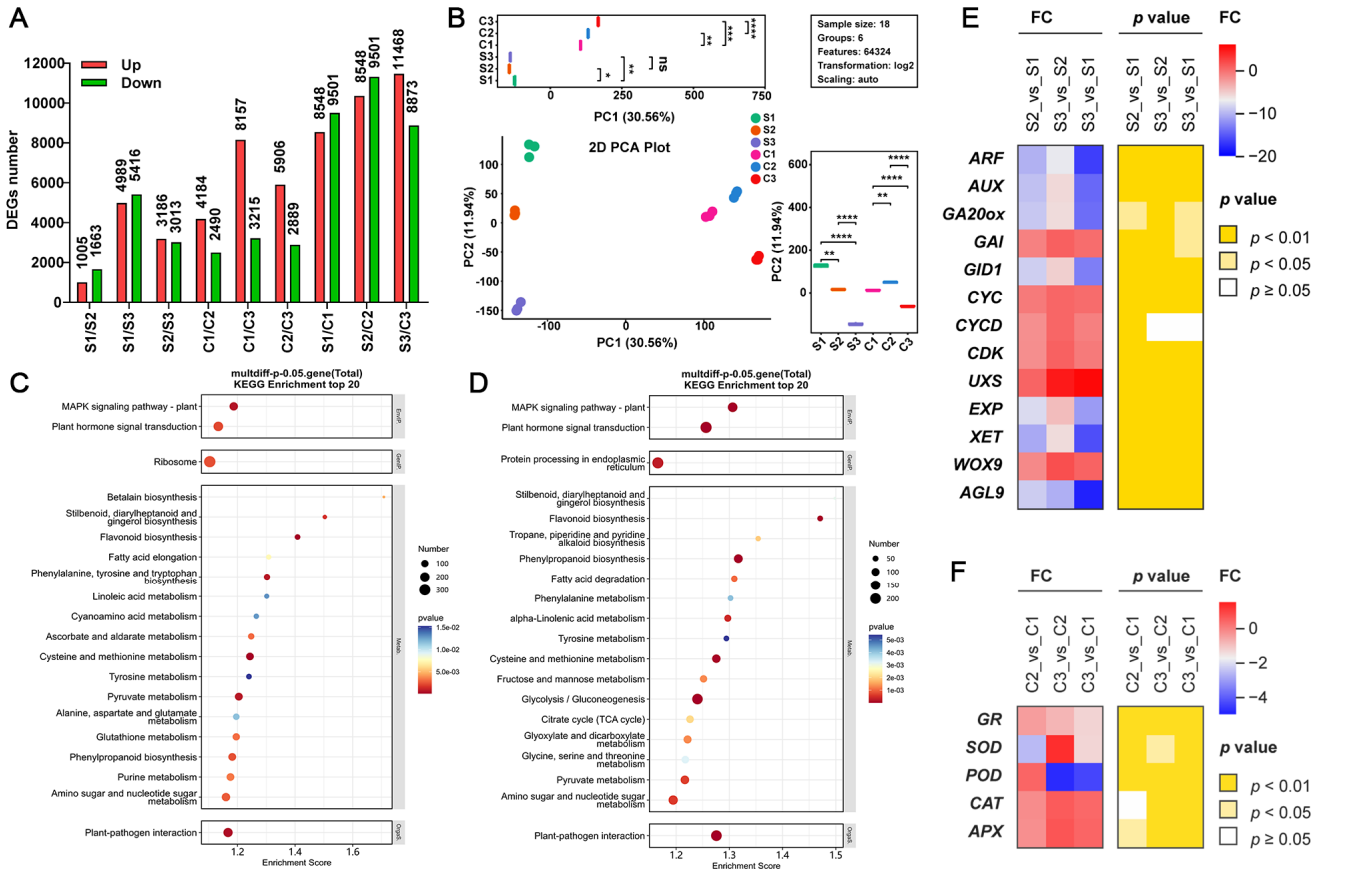


Figure 2. Transcriptomic differences between pedicels and pedicel-derived calli. (**A**) Number of DEGs identified in pairwise comparisons between sample groups. (**B**) The principal component analysis (PCA) of the transcriptome profiles. Percentages indicate the variance explained by principal components 1 (PC1) and PC2. * ($p < 0.05$), ** ($p < 0.01$), *** ($p < 0.001$), and **** ($p < 0.0001$) indicate significance levels, and ns indicates no significance. (**C**) Representative significantly enriched KEGG pathways in pedicel samples (S1, S2, S3) comparisons, bar and bubble plots show significantly enriched KEGG pathways, hereinafter the same. (**D**) Representative significantly enriched KEGG pathways in pedicel-derived callus (C1, C2, C3) sample comparisons. (**E**) Relative expression levels of DEGs in pedicel samples (S1, S2, S3). (**F**) Relative expression levels of DEGs in pedicel-derived callus (C1, C2, C3).

KEGG enrichment analysis clarified DEG functions in pedicel samples. Top enriched pathways included MAPK signaling pathway-plant, plant hormone signal transduction, ribosome, amino acid (phenylalanine/tyrosine/tryptophan) biosynthesis, flavonoid biosynthesis, plant–pathogen interaction, and metabolism (cysteine/methionine, phenylpropanoid, purine) among S1, S2 and S3 (Figure 2C). In callus samples, DEGs were enriched in pathways including MAPK signaling pathway-plant, plant hormone signal transduction, endoplasmic reticulum protein processing, flavonoid biosynthesis, glycolysis/gluconeogenesis, alpha-linolenic acid metabolism, and sugar (amino/nucleotide) metabolism among C1, C2 and C3 (Figure 2D).

To further characterize pedicel- and callus-related transcript expression, we profiled DEGs from the enriched pathways by using qRT-PCR. In pedicel samples (S1, S2, S3), genes such as *ARF*, *Auxin/IAA* (*AUX*), *GA 20-oxidase* (*GA20ox*), *gibberellin insensitive dwarf 1* (*GID1*), *expansin* (*EXP*), *xyloglucan endotransglycosylase* (*XET*), and *agamous-like 9* (*AGL9*) showed a decreasing expression trend from S1 to S3. Conversely, genes including *gibberellin insensitive* (*GAI*), *cyclin* (*CYC*), *cyclin D* (*CYCD*), *cyclin-dependent kinase* (*CDK*), *UDP-glucuronic acid decarboxylase* (*UXS*), and *WUSCHEL-related homeobox 9* (*WOX9*) exhibited an increasing

expression trend from S1 to S3 (Figure 2E). Overall, DEGs related to hormone signaling and cell expansion-associated genes (e.g., *ARF*, *AUX*, *EXP*, *XET*) were downregulated while growth regulation and cell cycle-related genes (e.g., *CYC*, *CDK*) were upregulated across the S1 to S3 stages. Whereas in callus samples, the expression levels of *glutathione reductase* (*GR*) and *superoxide dismutase* (*SOD*) showed a decreasing trend from C1 to C3. In contrast, *peroxidase* (*POD*), *ascorbate peroxidase* (*APX*), and *catalase* (*CAT*) displayed an increasing expression trend from C1 to C3 (Figure 2F). The expression patterns of antioxidant enzymes varied significantly across different callus samples, reflecting the dynamic modulation of the antioxidant system in callus derived from pedicels at different developmental stages.

3.3. Metabolomic Analyses of Pedicels and Pedicel-Derived Calli

To identify DAMs, HCA and KEGG pathway enrichment analysis were performed on pedicels and pedicel-derived calli. Both LC-MS and GC-MS were used for comprehensive metabolite detection. Within each group, samples clustered closely, indicating high metabolic homogeneity among biological replicates (Figure 3).

For LC-MS-identified DAMs, distinct abundance patterns were observed among pedicel samples. (R)-(+)-2-Pyrrolidone-5-carboxylic acid was abundant in S2 but scarce in S3, while D-maltose showed the opposite trend. Metabolites like β-chlorogenin 3-[4-(2-glucosyl-3-xylosylglucosyl) galactoside] (β-chlorogenin), D-(+)-malic acid, thidiazuron (TDZ), and maritimein also exhibited group-specific differences, potentially serving as biomarkers (Figure 3A). Among the DAMs identified by GC-MS in the pedicel group, glucose was abundant in the S2 and S3 groups and scarce in the S1 group, while D-fructose showed the opposite pattern. Compounds such as L-asparagine and sucrose also had distinct abundance patterns, which might play crucial roles in the metabolic differences among the S1, S2, and S3 groups (Figure 3B). Enriched pathways among pedicels included energy metabolism (galactose metabolism, citrate cycle), amino acid/nucleotide processing (aminoacyl-tRNA biosynthesis, pentose phosphate pathway), stress responses (ascorbate/aldarate metabolism), and lipid signaling (linoleic acid metabolism) (Figure 3C).

In callus samples, LC-MS-detected metabolites clustered distinctly by abundance across C1, C2, and C3. In C1, sucrose, L-arginine, and TDZ were abundant, while ethylvanillin glucoside was low. C2 had high levels of β-chlorogenin, cellulose and L-isoleucine, but low isocitrate and citric acid. C3 showed elevated citric acid, L-oxalylalbizziine, and ethylvanillin glucoside, with reduced cellulose, benzyl gentiobioside, sucrose, and L-arginine (Figure 3D). GC-MS analysis also highlighted metabolite variations: C1 was rich in L-tyrosine, L-alanine, and D-fructose but low in D-(+)-mannose and D-ribofuranose; C2 had high L-histidine, L-lysine, and L-glutamine, with low citric acid and D-fructose; C3 featured high citric acid, and low 2-propylmalonic acid, galactose 1-phosphate and D-galactose 6-phosphate (Figure 3E). Top enriched KEGG pathways involved carbohydrate metabolism (galactose metabolism, citrate cycle, glyoxylate and dicarboxylate metabolism), amino acid metabolism and activation (aminoacyl-tRNA biosynthesis, arginine and proline metabolism, cysteine, and methionine metabolism), transport mechanisms (ABC transporters) (Figure 3F).

3.4. Integrative Transcriptomic and Metabolomic Analysis of Pedicels

Since S1, S2 and S3 are consecutive key developmental stages, we performed an integrative transcriptomic–metabolomic analysis to reveal the dynamic regulatory crosstalk between gene expression and metabolite accumulation during their transition.

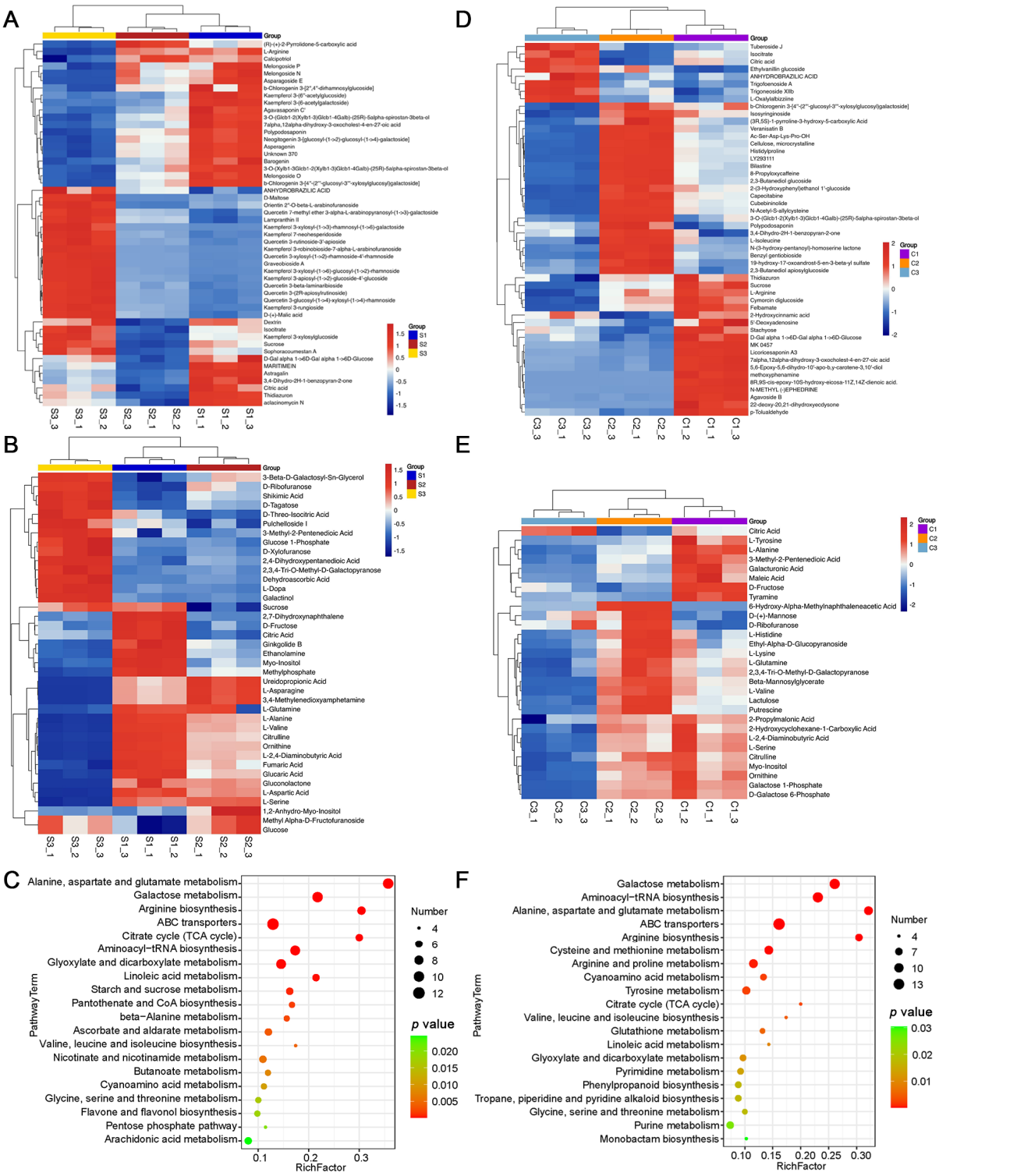


Figure 3. Metabolomic profiling and pathway analysis of pedicels and pedicel-derived calli. (**A**) Hierarchical clustering analysis (HCA) of DAMs detected by LC-MS in pedicel samples (S1, S2, S3). (**B**) HCA of DAMs identified by GC-MS in pedicel samples (S1, S2, S3). (**C**) KEGG pathway enrichment analysis of DAMs for pedicel samples (S1, S2, S3). (**D**) HCA of LC-MS-derived DAMs in callus samples (C1, C2, C3). (**E**) HCA of GC-MS-detected DAMs in callus samples (C1, C2, C3). (**F**) KEGG pathway enrichment analysis of DAMs for callus samples (C1, C2, C3).

Integrative transcriptomic–metabolomic analysis of S1 and S2 showed distinct pathway enrichment at metabolite and RNA levels, reflecting complex regulatory mechanisms (Figure 4A,B). Pathways like phenylpropanoid biosynthesis, flavonoid biosynthe-

sis, cyanamino acid metabolism, and nitrogen metabolism were transcriptionally dominant. In contrast, glyoxylate and dicarboxylate metabolism, galactose metabolism, and starch and sucrose metabolism were enriched at both levels, indicating coordinated metabolic-transcriptional responses (Figure 4A). We constructed a metabolic pathway interaction network for the S1/S2 comparison. Carbohydrate metabolism pathways (glycolysis/gluconeogenesis, TCA cycle, pyruvate metabolism) act as central hubs, interacting extensively with amino acid, lipid, and nucleotide pathways to orchestrate energy and biosynthesis. Amino acid pathways (e.g., alanine/aspartate/glutamate, glycine/serine/threonine metabolism) show broad connectivity, which link to carbohydrate pathways. Plant hormone signal transduction reveals metabolism-signaling crosstalk, suggesting hormones mediate metabolic reprogramming (Figure 4B). Overall, the S1/S2 network features a carbohydrate-centered metabolic framework integrating amino acid metabolism and hormonal signaling, supporting the energetic/biosynthetic demands of physiological state shifts (Figure 4B).

Likewise, integrative transcriptomic–metabolomic analysis of the S2/S3 comparison was performed (Figure 4C,D). The results uncovered that, metabolite-driven pathways including the TCA cycle and amino acid metabolism exhibited significant enrichment, directly catering to immediate energetic and biosynthetic requirements. Conversely, phenylpropanoid and flavonoid biosynthesis displayed robust enrichment at the RNA level (Figure 4C). Carbohydrate pathways (e.g., glycolysis/gluconeogenesis, TCA cycle) serve as core hubs, interacting extensively with amino acid, lipid, and nucleotide pathways to regulate energy flux and biosynthesis, thus supporting S2/S3 stage transition. Amino acid pathways (e.g., alanine, aspartate and glutamate metabolism) link to carbohydrate pathways, which integrate energy and nitrogen metabolism. Notably, phenylpropanoid biosynthesis connects to core networks, indicating specialized metabolite reprogramming, while nucleotide pathways interact with amino acid pathways to support growth and response processes (Figure 4D).

Both S1/S2 and S2/S3 relied on a carbohydrate-centered metabolic framework, with amino acid metabolism as a key integrator and phenylpropanoid/flavonoid biosynthesis showing strong transcriptional activity. However, S1/S2 exhibited broader metabolic-transcriptional coordination across multiple pathways and integrated hormonal signaling, while S2/S3 focused on specialized metabolic reprogramming via phenylpropanoid biosynthesis and enhanced nucleotide-amino acid crosstalk, highlighting stage-specific regulatory patterns during pedicel development.

3.5. Integrative Transcriptomic and Metabolomic Analysis of Calli

Consistent with the pedicel samples, integrative transcriptomic–metabolomic analysis between C1 and C2 was performed (Figure 5A,B). At the metabolic level, galactose metabolism, ABC transporters, citrate cycle (TCA cycle), and plant hormone signal transduction showed distinct enrichment patterns. Top RNA-enriched pathways included phenylpropanoid biosynthesis, ABC transporters, TCA cycle, alanine/aspartate/glutamate metabolism, phenylalanine/tyrosine/tryptophan biosynthesis, flavonoid biosynthesis, and linoleic acid metabolism (Figure 5A). The C2/C1 comparison pathway network shows integrated metabolic and regulatory connections. Central carbohydrate metabolism (TCA cycle, glycolysis/gluconeogenesis, pentose phosphate pathway) acts as a hub, linking to amino acid (e.g., alanine/aspartate/glutamate, aromatic amino acid biosynthesis) and nucleotide (e.g., purine) metabolism, coordinating carbon flow for energy and biosynthesis. Plant hormone signal transduction connects to metabolic nodes, reflecting hormone-mediated metabolic regulation. Lipid and cofactor/vitamin metabolism also integrate with cen-

tral pathways. Overall, it reveals an interdependent system where energy metabolism, biosynthesis, and signaling are co-regulated in C2/C1 comparison (Figure 5B).

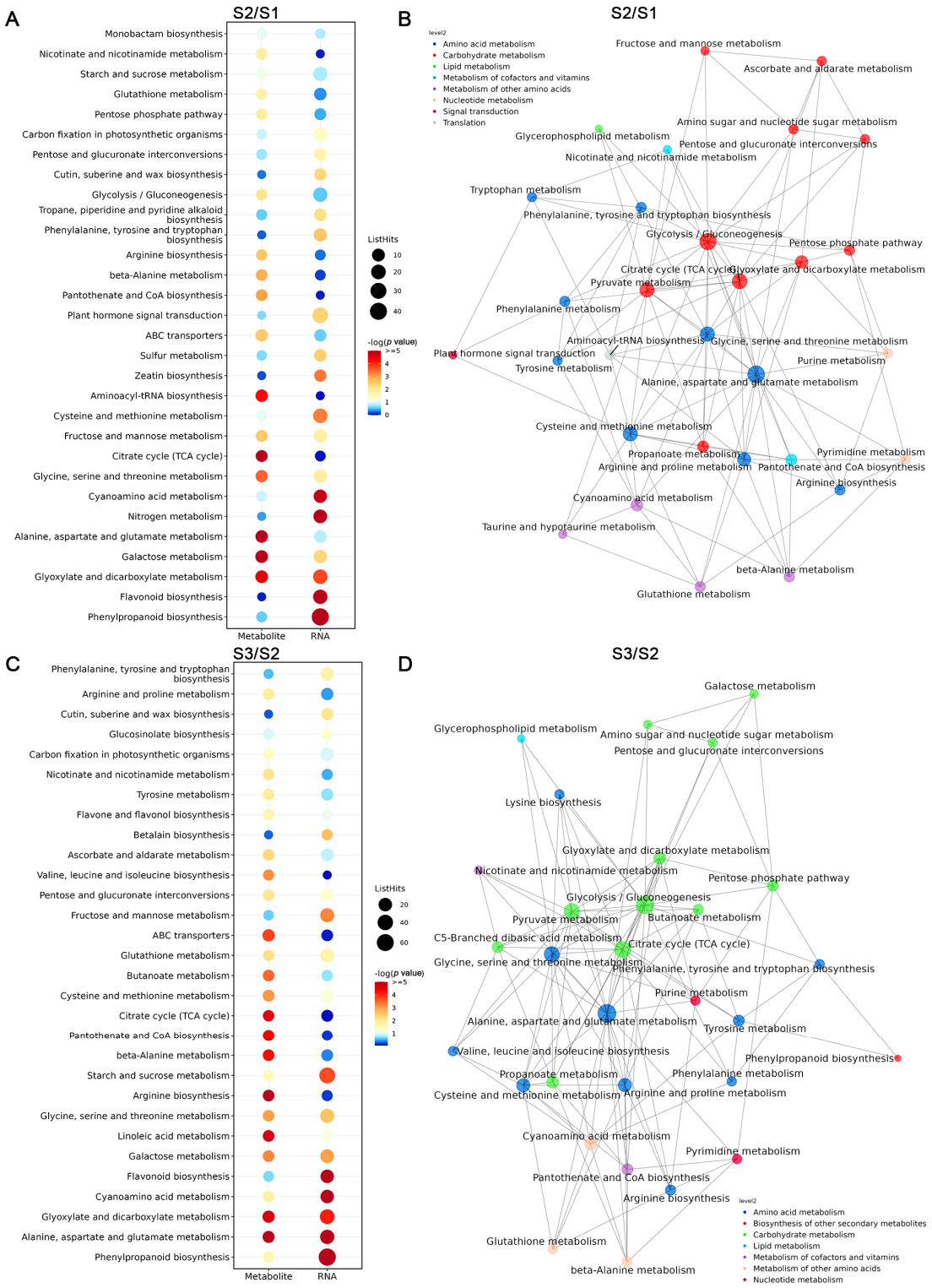


Figure 4. Integrative transcriptomic–metabolomic analysis of pedicels. (**A**) Pathway enrichment divergence patterns between transcriptomic and metabolomic profiles in the S2/S1 comparison. (**B**) Transcript–metabolite correlation network for the S2/S1 comparison. (**C**) Pathway enrichment divergence between transcriptomic and metabolomic profiles in the S3/S2 comparison. (**D**) Transcript–metabolite correlation network for the S3/S2 comparison.

For the C3/C2 comparison, an integrative transcriptomic–metabolomic analysis was performed (Figure 5C,D). At the metabolic level, galactose metabolism, alanine/aspartate/glutamate metabolism, arginine/proline metabolism, and ABC transporters showed distinct enrichment patterns. Top transcriptomically enriched pathways included phenylpropanoid biosynthesis, plant hormone signal transduction, galactose metabolism, starch/sucrose metabolism, flavonoid biosynthesis, and linoleic acid metabolism (Figure 5C). The C3/C2 comparison pathway network presents the following features: Central carbohydrate metabolism (glycolysis/gluconeogenesis, TCA cycle, pentose phosphate pathway) serves as the core, tightly linking to amino acid biosynthesis (e.g., alanine/aspartate/glutamate, phenylalanine/tyrosine/tryptophan) and nucleotide metabolism (purine/pyrimidine pathways). Plant hormone signal transduction directly connects to metabolic nodes. Amino acid metabolism (e.g., lysine, cysteine/methionine) links with aminoacyl-tRNA biosynthesis (Figure 5D).

The integrative analysis of C2/C1 and C3/C2 comparisons reveals a universal regulatory foundation centered on central carbohydrate metabolism (TCA cycle, glycolysis, pentose phosphate pathway) and plant hormone signaling. While C2/C1 exhibits specificity through enriched secondary metabolism (phenylpropanoid/flavonoid biosynthesis) and ABC transporters, mediating carbon–amino acid–lipid coordination, and C3/C2 comparison is distinguished by tRNA–metabolism coupling (aminoacyl-tRNA biosynthesis) and restructured galactose metabolism, optimizing translational capacity and carbon allocation. Both systems demonstrate co-regulated energy provisioning, stress defense, and growth.

3.6. Differential Metabolic Pathway Enrichment Analysis

Integrating with previous analyses on the effects of pedicel explant developmental stages on callus induction and proliferation, we performed a comparative analysis of metabolic pathways (Figure 6). This heatmap visualizes pathway enrichment across the developmental comparisons of S1/S2, S2/S3, C1/C2, and C2/C3, and we further identified pathways coordinated at both the transcriptomic and metabolomic levels.

At the DEG-based transcriptomic level, all comparisons showed significant enrichment for phenylpropanoid biosynthesis, flavonoid biosynthesis, stilbenoid, diarylheptanoid and gingerol biosynthesis, fatty acid elongation, and zeatin biosynthesis. S1/S2 and S2/S3 specifically showed enrichment for nitrogen metabolism, cyanoamino acid metabolism, glyoxylate and dicarboxylate metabolism. C1/C2 and C2/C3 specifically showed enrichment for linoleic acid metabolism, plant–pathogen interaction, MAPK signaling pathway-plant, alpha-linolenic acid metabolism, diterpenoid biosynthesis, and plant hormone signal transduction (Figure 6A).

At the metabolic level, all comparisons showed significant enrichment for alanine/aspartate/glutamate metabolism, galactose metabolism, citrate cycle (TCA cycle), glyoxylate and dicarboxylate metabolism, aminoacyl-tRNA biosynthesis, butanoate metabolism, valine/leucine/isoleucine biosynthesis, arginine biosynthesis, ABC transporters, and glutathione metabolism. S1/S2 and S2/S3 specifically showed enrichment for pantothenate and coA biosynthesis, beta-alanine metabolism, glycolysis/gluconeogenesis, and ascorbate and aldarate metabolism. C1/C2 and C2/C3 specifically showed enrichment for plant hormone signal transduction (Figure 6B).

Integrating RNA and metabolic level data (Figure 6) reveals that plant hormone signal transduction was specifically enriched during callus developmental stages at both levels, highlighting the core regulatory role of plant hormone signal transduction in maintaining callus developmental status. In contrast, fundamental energy and nutritional metabolic pathways such as the TCA cycle (energy metabolism) and amino acid biosynthesis (nutritional synthesis) were ubiquitously enriched across all developmental comparisons.

Thus, hormone signaling acts as the key direct regulator of callus status, while nutritional metabolism offers supportive and foundational roles.

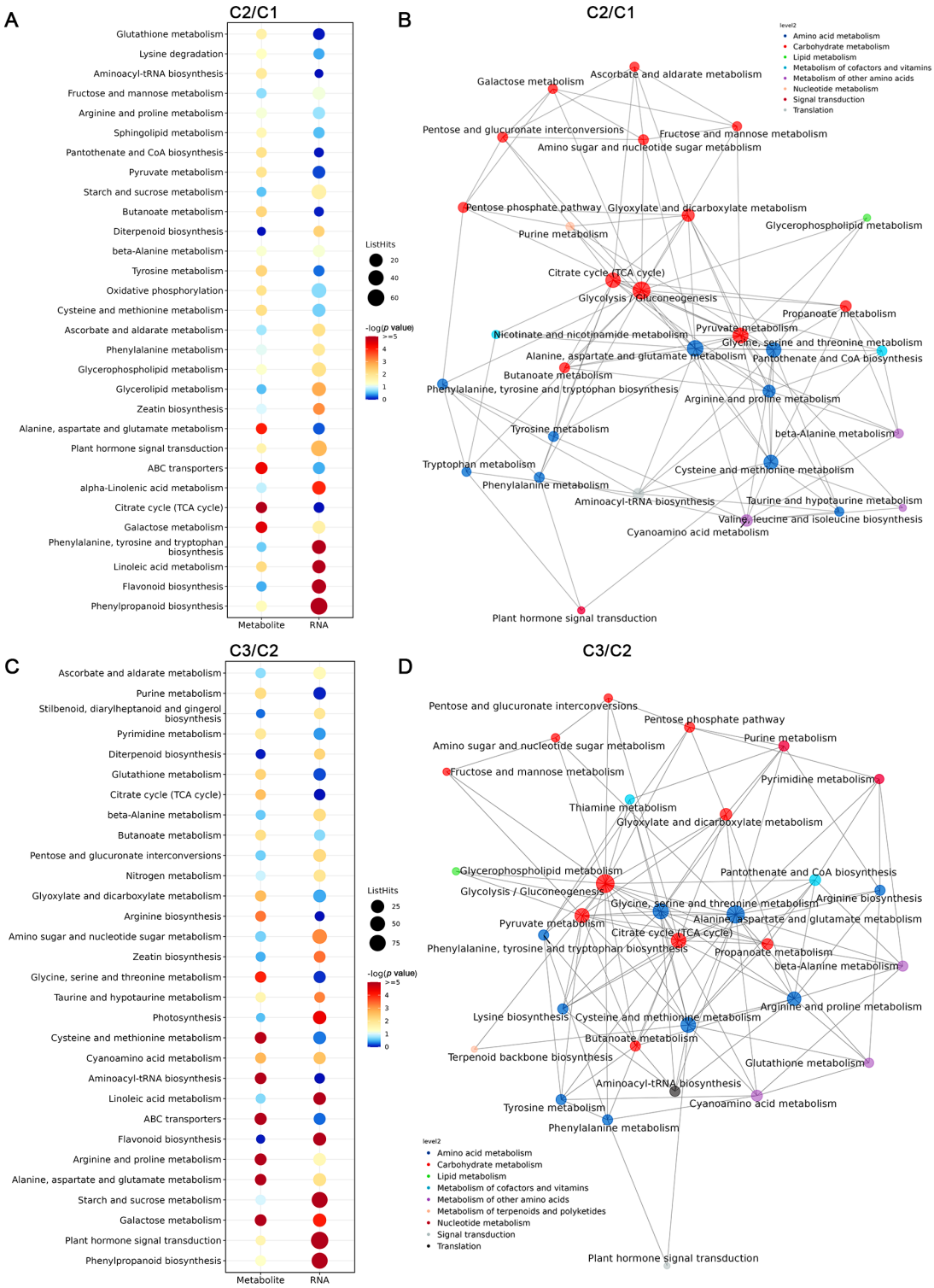


Figure 5. Integrative transcriptomic–metabolomic analysis of pedicel-derived calli. (**A**) Pathway enrichment divergence patterns between transcriptomic and metabolomic profiles in the C2/C1 comparison. (**B**) Transcript–metabolite correlation network for the C2/C1 comparison. (**C**) Pathway enrichment divergence patterns between transcriptomic and metabolomic profiles in the C3/C2 comparison. (**D**) Transcript–metabolite correlation network for the C3/C2 comparison.

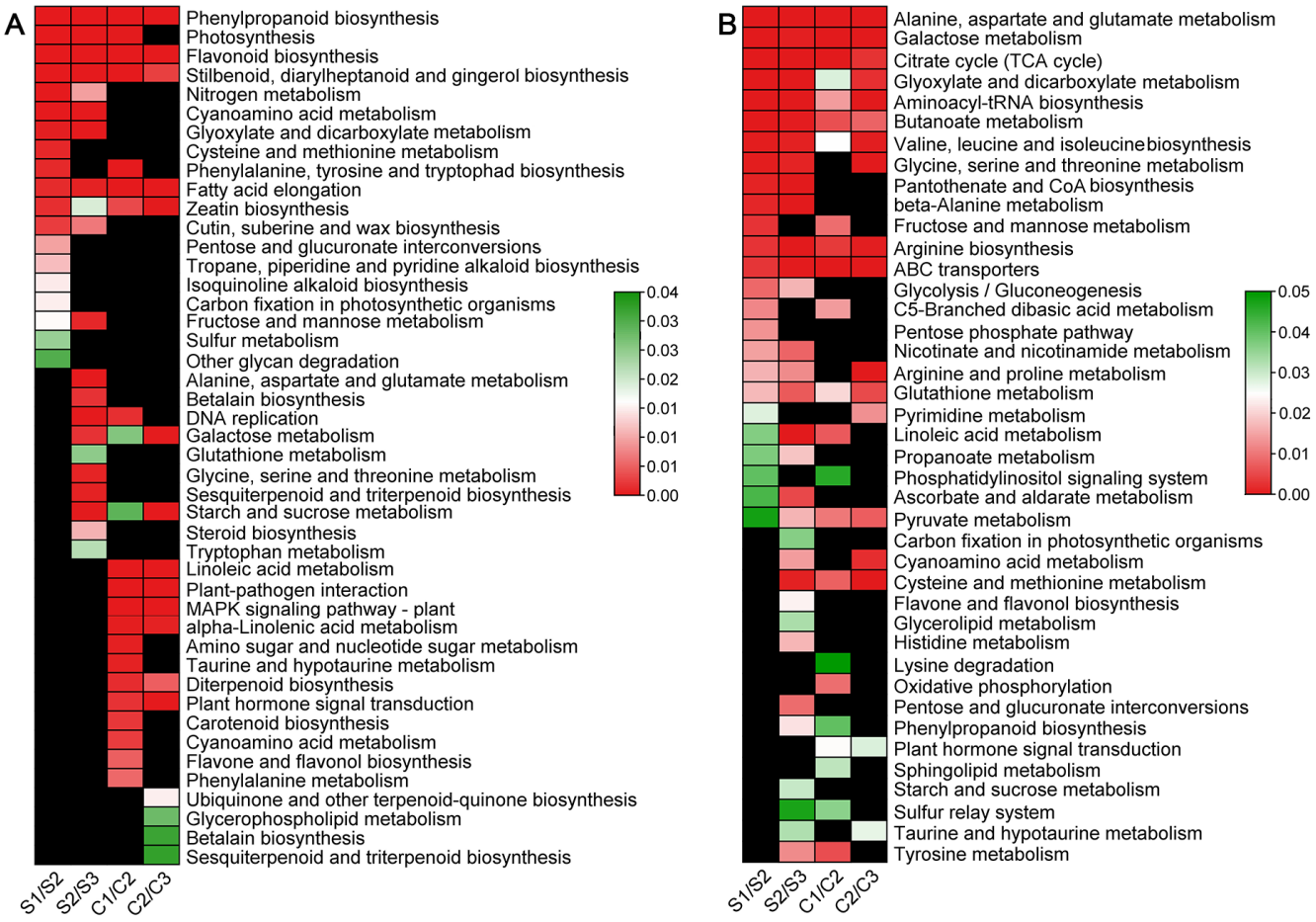


Figure 6. Pathway enrichment heatmap of comparative metabolomic groups. (**A**) DEGs involved in pathways among comparisons. (**B**) DAMs involved in pathways among comparisons. Bars denote significance levels. Color intensity indicates the significance of the pathway enrichment, with black representing no significant difference and $p < 0.05$ set as the significance threshold.

3.7. WGCNA of Pedicel and Callus Samples

To elucidate the associations between gene co-expression modules and phenotypic traits, we performed WGCNA. A hierarchical clustering dendrogram of gene co-expression patterns was constructed (Figure 7A). Using dynamic branch cutting and module merging algorithms, we partitioned genes into distinct co-expression modules. A module–trait relationship heatmap was then constructed to identify significant associations between specific modules and target phenotypes (Figure 7B). Notably, the darkmagenta module exhibited a strong positive correlation with trait C2 ($r = 0.84$, $p < 0.001$), while the pink module showed a significant negative correlation with trait S3 ($r = -0.67$, $p < 0.01$). Correlation coefficients and statistical significance metrics revealed potential regulatory relationships. From modules demonstrating significant trait associations, we further extracted and visualized five core gene co-expression networks (Figure 7C–G). The darkmagenta module network (726 genes) featured interactions among genes such as CDK and CDC20, implicating G2/M phase-specific cyclin-mediated cell cycle control, indicating the module's involvement in vigorous cell division processes (Figure 7C). The black module network (3098 genes), including MPG and components of the queuosine salvage pathway, interacted and were associated with metabolic salvage and mitochondrial functions (e.g., MRPS10), reflecting its role in metabolic homeostasis (Figure 7D). The cyan module network (12,924 genes) involved interactions among genes such as malate synthase and defensin, which are associated with defense responses and secondary metabolism, highlighting the module's

function in stress response (Figure 7E). The dark gray module network (12,630 genes) encompassed transcription factors and regulatory genes (e.g., RAV6, LHW), covering hormone signaling (e.g., JAZ), and protein phosphorylation (e.g., PPA2). This reveals their roles in signal transduction and transcriptional regulation (Figure 7F). The pink module network (1762 genes) featured peroxidase genes, which are key regulators of oxidative stress responses. Interestingly, S1 and S3 exhibited positive ($r = 0.77$, $p < 0.0001$) and negative correlations ($r = -0.67$, $p < 0.001$) with this module, respectively (Figure 7G).

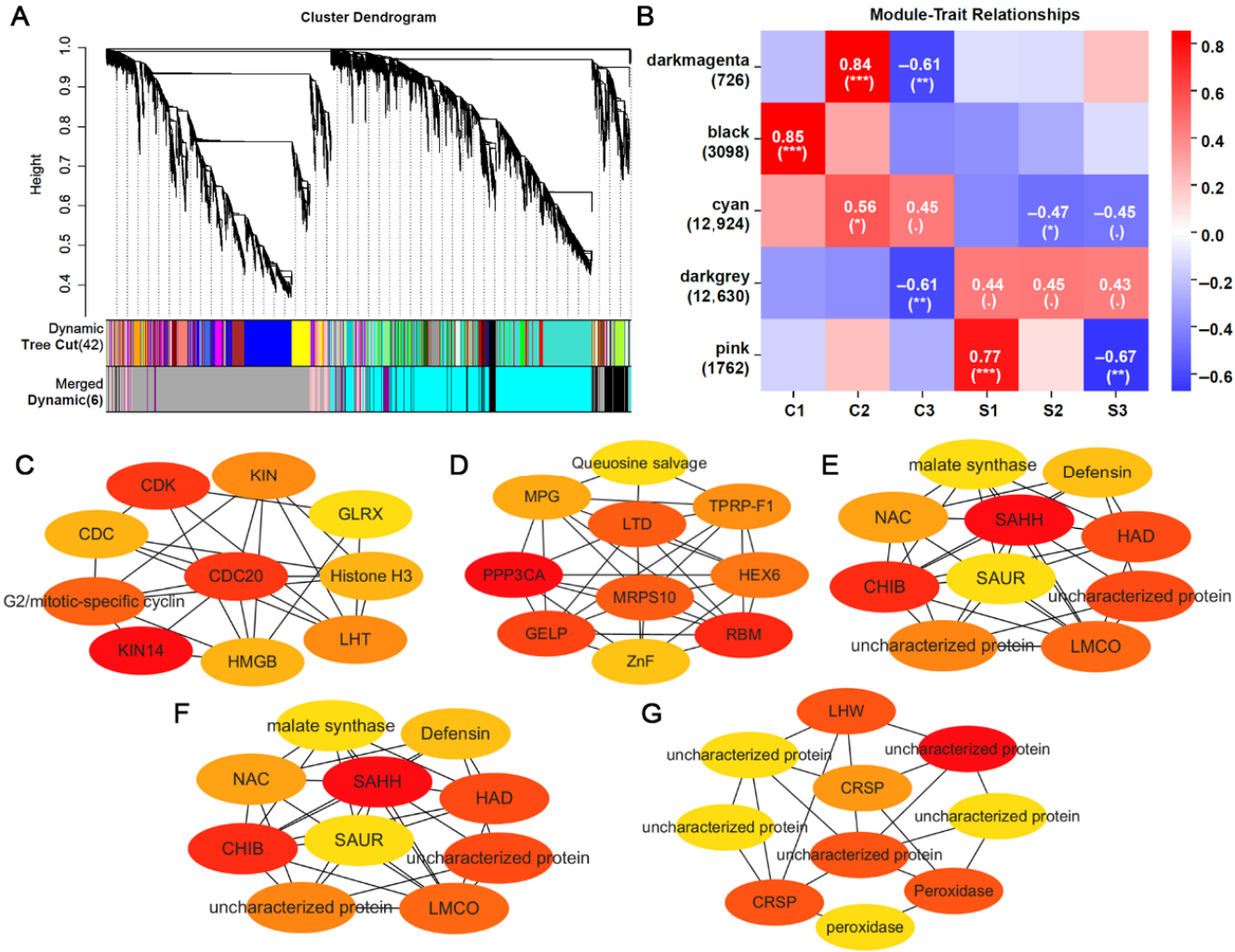


Figure 7. WGCNA: module clustering, trait associations, and hub gene networks. (**A**) Cluster dendrogram: Illustrates the hierarchical clustering of genes, where branch height reflects the dissimilarity in gene expression patterns. The colored strips below represent the identified gene modules. (**B**) Module–trait association heatmap: Rows correspond to gene modules (with the number in parentheses indicating the gene count per module), and columns represent different traits. Color intensity and values denote the correlation coefficients between modules and traits (red for positive correlation, blue for negative correlation). Significance levels are marked with asterisks (*** for $p < 0.001$, ** for $p < 0.01$, * for $p < 0.05$, and · for no significance). (**C**) Co-expression network of hub genes in the darkmagenta key module: Each node represents a gene, and edges indicate significant co-expression relationships. This network highlights genes with central roles (hub genes) in the module. (**D**) Co-expression network of hub genes in the black key module. (**E**) Co-expression network of hub genes in the cyan key module. (**F**) Co-expression network of hub genes in the dark gray key module. (**G**) Co-expression network of hub genes in the pink key module.

4. Discussion

4.1. Regeneration Potential of Pedicel Developmental Stages

Traditional understanding posits that young explants are optimal for regeneration due to low differentiation and high metabolic activity [2,45]. However, based on comprehensive analysis of pedicel morphology, histological structure, callus induction rate, and multiplication efficiency, our study reveals that the semi-mature explant (S2) outperforms both immature (S1) and mature (S3) tissues, with a high callus induction rate and proliferation coefficient, which challenges the oversimplified notion that "the younger the explant, the better the regeneration" [46,47]. Our study identified S2 as the optimal explant for in vitro plant regeneration in *A. praecox*.

In plant tissue culture, unsterilized explants are highly susceptible to contamination, making sterilization a critical step [48]. In studies on *Malus* species, the contamination rate of explants is the lowest in spring and summer [45]. The sampling season of pedicels in this study is relatively consistent with that of *Malus* species. The semi-mature pedicel exhibits a semi-differentiated structure, characterized by enlarged parenchymal cells and incompletely dispersed vascular bundles. This structural advantage addresses a core contradiction in explant regeneration [49,50]. It enables the efficient transport of exogenous PGRs (e.g., PIC) and nutrients while retaining cell division potential [51], which resolves the trade-off between mitotic activity and stress responsiveness. For S1, the cells possess strong meristematic capacity and robust plant hormone signal transduction activity, with high expression of auxin-related (e.g., *ARF*, *AUX*), GA-related (e.g., *GA20ox*, *GID1*), and cell wall expansion-related (e.g., *EXP*, *XET*) genes, while the accumulation of starch grains and TDZ provides energy and PGRs reserves for maturation and differentiation (Figure 8). However, thin cell walls increase vulnerability to disinfection-induced rupture [48], triggering the massive release of phenolic compounds [52]; Coupled with high polyphenol oxidase (PPO) activity, this inhibits the formation and proliferation of callus [53,54]. In contrast, S3's over-lignified vascular bundles form a physical barrier that blocks cell wall remodeling, with high expression of GA signaling negative regulator (e.g., *GAI*), and cell wall synthesis-related (e.g., *UXS*) genes, inhibiting dedifferentiation initiation and resulting in calli with low proliferation [55]. Gene co-expression modules, characterized by complex internal interactions, are significantly associated with core biological processes including cell cycle progression, metabolic homeostasis, and defense responses. Interestingly, in terms of oxidative stress response, S2 is intermediate between S1 and S3, and this balanced state was demonstrated to exert a positive effect on its regeneration.

Cytological traits further amplified the regenerative advantages of the semi-mature pedicel-derived callus. C2 exhibits denser cytoplasm than C1, and this cytological feature provides sufficient energy for continuous cell division [10], the enrichment of cellulose and amino acids (e.g., L-isoleucine, L-histidine, L-lysine, L-glutamine) (Figure 8), translating to tangible functional benefits, with C2 showing a higher proliferation coefficient than C1 and C3. Furthermore, C2 showed high correlations with the modules of cell proliferation and stress response. In contrast, C1 suffers from energy deficiency due to thin cytoplasm, while callus from mature pedicels, though spherical in shape, has thin cytoplasm, resulting in the weakening of regenerative potential [55]. The magnitude of transcriptional variation (DEG number) is positively correlated with the developmental distance between the compared samples. Notably, C1 shows high levels of sucrose and L-arginine, but low levels of ethylvanillin glucoside; in contrast, C3 exhibits a completely opposite trend (Figure 8).

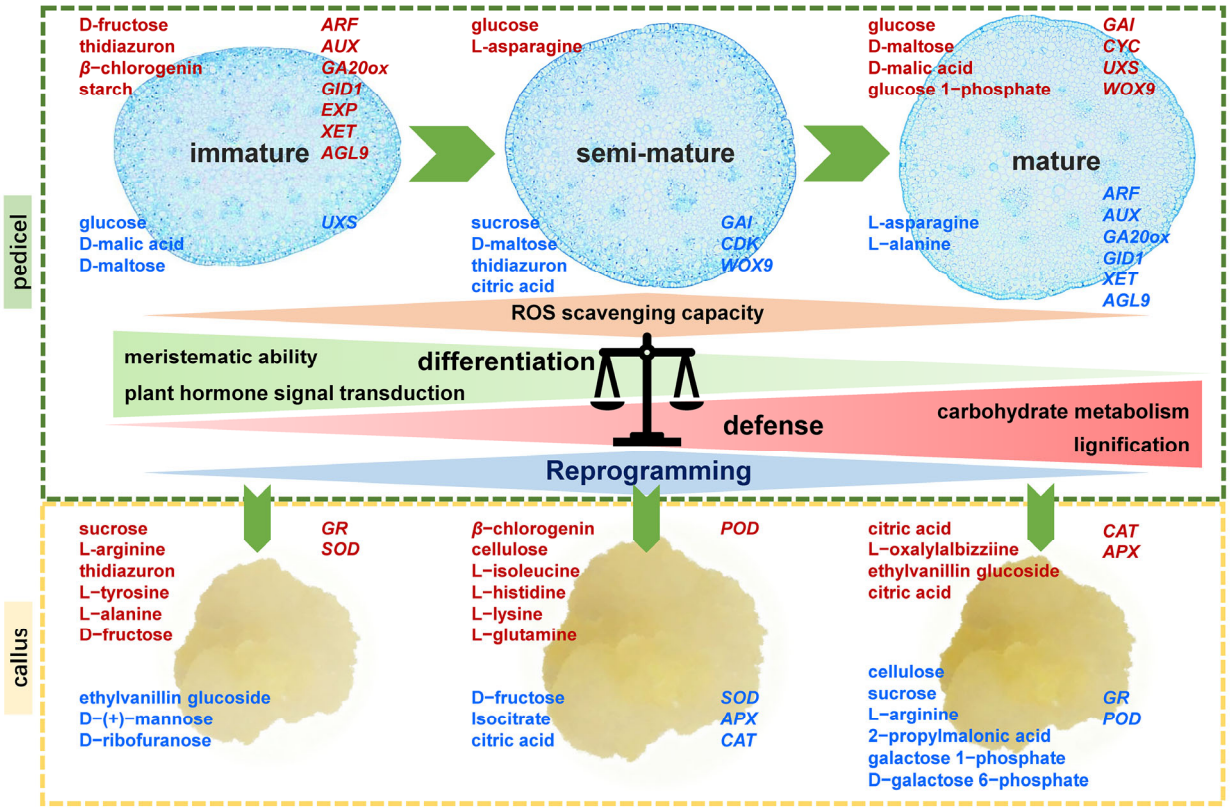


Figure 8. Hypothetical model diagram of the acquisition of regenerative potential of pedicels in *A. praecox*. Red indicates the upregulation of DEGs or increase in DAMs, while blue indicates the downregulation of DEGs or decrease in DAMs. Metabolites are represented in regular type, and genes are represented in italic type. The swallowtail arrow indicates the direction of development.

Based on our research results on the developmental stages of *A. praecox* pedicels, we conclude that callus induction in *A. praecox* follows the "developmental window" theory, which holds that only explants at specific ages or developmental stages possess strong regenerative potential [7]. The S2 during *A. praecox* pedicel sampling serves as a developmental window for callus induction, and its core feature lies in the dynamic balance between the differentiation status and metabolic activity of explants [16]. It is precisely this balance that maximizes the regenerative potential of explants at this stage. This conclusion suggests that in plant in vitro culture, the precise identification of specific developmental stages, rather than arbitrarily selecting young tissues as explants, could prove an effective strategy for optimizing in vitro culture efficiency across diverse plants [56,57].

4.2. Metabolic–Epigenetic Synergy: Molecular Carriers of Developmental Memory

The high regenerative capacity of S2 pedicels originates from the synergistic regulation of metabolic networks and epigenetic modifications [58–60], which together construct a molecular microenvironment defined by sufficient energy and moderate defense [27].

In terms of metabolic balance, S2 establishes a unique equilibrium that supports regeneration. For energy supply, S2 enriches glucose and L-asparagine, and has fewer TCA cycle intermediates (e.g., citric acid) and a lower sucrose content than both S1 and S3. Notably, ascorbate and aldarate metabolism among the samples was significantly enriched, indicating that S2 has strong antioxidant capacity, which can serve as a marker for high regenerative potential [27]. For defense balance, C2 moderately activates the phenylpropanoid pathway, with higher β-chlorogenin and cellulose accumulation. APX, a key enzyme in the ascorbic acid (AsA)-glutathione cycle, indirectly inhibits browning

by maintaining AsA content to suppress PPO activity. It also directly blocks browning initiation by specifically scavenging hydrogen peroxide (H_2O_2), thereby preventing ROS-induced PPO activation and membrane damage [61].

Epigenetic modifications further reinforce S2's regenerative advantage by maintaining chromatin accessibility [58]. These genes remodel chromatin to keep dedifferentiation-related genes in an open state [62], promoting their expression. Additionally, S2 specifically accumulates (R)-(+)-2-pyrrolidone-5-carboxylic acid (Figure 3A), an inhibitor of DNA methyltransferase [63]. This metabolite synergizes with C2's hypomethylated state to enhance cell reprogramming. WGCNA identified a darkmagenta module that is strongly correlated with C2; this module is enriched in genes associated with vigorous cell division and histone modification. A core gene in this module is *histone H3*, and it was reported that *OsLEC1* influences callus induction via histone acetylation modification in rice [64].

Notably, metabolism and epigenetics are not independent regulatory layers, and they interact via a hormone–energy axis [65]. Transcriptomic–metabolomic integration revealed synchronized enrichment of the hormone signaling pathway and carbohydrate metabolism during the S2 to C2 transition. In plant tissue culture, callus formation is induced by high auxin concentrations [66]. High levels of IAA seemed to be responsible for the highest frequency of regeneration in *Begonia tuberosa* [67]. Exogenous PIC further activated this axis, which aligns with S2′s balanced endogenous hormone levels. This model, in which metabolism provides the material basis, epigenetics regulates gene expression, and hormones coordinate crosstalk, constitutes the core of S2′s high regenerative capacity [68].

4.3. Molecular Barriers of Developmental Stages and Cross-Species Implications

The lower regeneration capacity of pedicels at stages S1 and S3 is attributed to stage-specific molecular barriers, and the underlying mechanisms of these barriers also account for cross-species differences in regenerative potential.

In *B. tuberosa*, low levels of anthocyanins and phenolics were detected in explants which showed stronger regenerative capacity [67]. For the S1 stage, excessive accumulation of flavonoids not only induced browning [69,70] but also modulated the activity of auxin-transporting P-glycoproteins [71]. Concurrently, genes related to glycolysis exhibit lower FPKM values than those at the S2 stage. This exacerbates energy scarcity and further suppressed the dedifferentiation process [72].

For the S3 stage, the primary barrier lies in lignin deposition. Specifically, S3 exhibited significantly higher lignin biosynthesis activity than S2, resulting in excessive lignification. This excessive lignification formed irreversible structural barriers to dedifferentiation [73]. Furthermore, genes including *GAI* and *UXS* are highly expressed, which are related to GA negative regulation and hemicellulose biosynthesis. In contrast, the expression of auxin signaling genes (*ARF*, *AUX*) and cell wall modification genes (*XET*) is downregulated (Figure 8). These changes collectively restrict its meristematic capacity and cell reprogramming potential.

These mechanisms are consistent with regenerative patterns across different plant taxa. Herbaceous plants with high regenerative potential (e.g., *Papaver rhoeas*) exhibited metabolic plasticity similar to that of S2-stage pedicels, including an active TCA cycle, lower sucrose/glucose ratio and moderate phenylpropanoid metabolism activity (Figure 8) [1]. In contrast, woody plants with poor regeneration capacity (e.g., *Camellia sinensis*) displayed S3-like traits, such as extensive lignification, TCA cycle blockage, and epigenetic locking [15].

Building on these findings, we established a regulatory model characterized by the hormone-energy axis, where the synchronized activation of hormone signaling and carbohydrate metabolism drove cell differentiation and proliferation (Figure 8). This

study identified the S2-stage pedicels of *A. praecox* as the optimal explants suitable for commercial propagation.

5. Conclusions

The regenerative potential of *A. praecox* pedicels is shaped by developmental stages and synergistically regulated by metabolic reprogramming, epigenetic imprinting, and hormone signaling. The semi-mature stage forms a unique molecular microenvironment, representing the optimal developmental stage for explant cell reprogramming to enhance in vitro propagation efficiency. Key metabolites play distinct roles: carbohydrates (glucose, sucrose, D-maltose) provide energy and carbon skeletons via carbohydrate metabolism to support meristematic capacity, cell differentiation, and reprogramming; amino acids (L-asparagine, L-arginine) facilitate nitrogen metabolism, protein synthesis, and stress defense to maintain explant viability; and specialized metabolites (TDZ, β-chlorogenin) mediate differentiation and stress tolerance. Physiologically, cell reprogramming induces callus, while meristematic capacity sustains proliferation and differentiation, and both processes are protected by ROS scavenging and defense mechanisms to mitigate culture-induced stress. Carbohydrate metabolism and plant hormone signal transduction are core pathways supplying essential resources and modulating propagation efficiency. This schematic provides actionable insights for optimizing the industrial-scale in vitro propagation of *A. praecox* and related crops.

Supplementary Materials: The following supporting information can be downloaded at https://www.mdpi.com/article/10.3390/horticulturae12010027/s1, Table S1: Primers used for qRT-PCR.

Author Contributions: Conceptualization, J.Y.; methodology, Y.D.; software, C.D.; validation, J.Y., and Y.D.; investigation, X.Y.; resources, J.Y.; data curation, C.D.; writing—original draft preparation, Y.D.; writing—review and editing, P.L.; visualization, H.W.; supervision, C.D.; project administration, J.Y.; funding acquisition, J.Y. All authors have read and agreed to the published version of the manuscript.

Funding: This research was funded by the Academic Core Teachers Program in Xinyang Agriculture and Forestry University (2022), the Young Key Teachers Training Program in Xinyang Agriculture and Forestry University (2021), and the Program of Research Fund for Young Teachers in Xinyang Agriculture and Forestry University (QN2022016, QN2023023).

Data Availability Statement: Data will be made on request.

Acknowledgments: We are grateful to Yakun Wang and Yun Teng for the experiments of microscopic observation.

Conflicts of Interest: The authors declare no conflicts of interest.

Abbreviations

The following abbreviations are used in this manuscript:

AGL9	Agamous-like 9
APX	Ascorbate peroxidase
ARF	Auxin response factor
AsA	Ascorbic acid
AUX	Auxin/IAA
CDC20	Cell Division Cycle 20
CDK	Cyclin-dependent kinase
CYC	Cyclin
CYCD	Cyclin D
Co	Cortex
DAMs	Differentially accumulated metabolites

DEGs	Differentially expressed genes
ddH_2O	Double-distilled water
EXP	Expansin
FC	Fold change
FDR	False discovery rate
FPKM	Fragments per kilobase per million mapped reads
GA	Gibberellin
GA20ox	GA 20-oxidase
GAI	Gibberellin insensitive
GID1	Gibberellin insensitive dwarf 1
GC-MS	Gas chromatography–mass spectrometry
GR	Glutathione reductase
H_2O_2	Hydrogen peroxide
HCA	Hierarchical cluster analysis
IAA	Indole-3-acetic acid
JAZ	Jasmonate ZIM-domain protein
KEGG	Kyoto Encyclopedia of Genes and Genomes
LC-MS	Liquid chromatography–mass spectrometry
MS	Mass spectrometry/Murashige and Skoog medium
Padj	Adjusted *p*-value
PCA	Principal component analysis
Pc	Parenchymal cell
PAS	Periodic acid-Schiff
PIC	Picloram
PGRs	Plant growth regulators
PPO	Polyphenol oxidase
QC	Quality control
ROS	Reactive oxygen species
SE	Standard error
SOD	Superoxide dismutase
St	Starch granule
TDZ	Thidiazuron
UXS	UDP-glucuronic acid decarboxylase
VIP	Variable importance in projection
Ve	Vessel
Vb	Vascular bundle
Epi	Epidermis
WOX9	WUSCHEL-related homeobox 9
WGCNA	Weighted gene co-expression network analysis

References

1. Aghaali, Z.; Hoshino, Y.; Monfared, S.R.; Moieni, A. Regulation of dedifferentiation and differentiation in different explants of *Papaver rhoeas* L. by one-step culture. *Sci. Hortic.* **2019**, *246*, 366–370. [CrossRef]
2. Aswathi, N.V.; Thomas, T.D. Direct and indirect shoot regeneration from leaf explants of *Centratherum punctatum* Cass., A wild ornamental plant. *Sci. Hortic.* **2023**, *320*, 112201. [CrossRef]
3. Li, J.; Na, X.; Qi, C.; Shi, R.; Li, K.; Jin, J.; Liu, Z.; Pu, M.; Wang, S.; Sun, H.; et al. Cytoplasmic G6PDs modulate callus formation in Arabidopsis root explants through regulation of very-long-chain fatty acids accumulation. *Plant Physiol. Biochem.* **2025**, *220*, 109526. [CrossRef]
4. Karakas, F.P. Efficient plant regeneration and callus induction from nodal and hypocotyl explants of goji berry (*Lycium barbarum* L.) and comparison of phenolic profiles in calli formed under different combinations of plant growth regulators. *Plant Physiol. Biochem.* **2020**, *146*, 384–391. [CrossRef]
5. Kavitha, N.; Saraswathi, M.S.; Kannan, G.; Bathrinath, M.; Backiyarani, S.; Uma, S. Development of direct regeneration protocol for mass multiplication of Musa spp. variety Udhayam (Pisang Awak, ABB) using different explants. *Sci. Hortic.* **2021**, *290*, 110506. [CrossRef]

6. Ma, J.; Li, Q.; Zhang, L.; Cai, S.; Liu, Y.; Lin, J.; Huang, R.; Yu, Y.; Wen, M.; Xu, T. High auxin stimulates callus through SDG8-mediated histone H3K36 methylation in Arabidopsis. *J. Integr. Plant Biol.* **2022**, *64*, 2425–2437. [CrossRef]
7. Mukherjee, E.; Gantait, S. Strawberry biotechnology: A review on progress over past 10 years. *Sci. Hortic.* **2024**, *338*, 113618. [CrossRef]
8. Fu, Z.; Yuan, X.; Li, Y.; Gao, J.; Wang, H.; Wang, X.; Wang, E.; Wang, L.; Zhang, H. Establishment of a complete in vitro micropropagation and plant regeneration system for *Paeonia suffruticosa* 'Hongxialanman' by inducing dormancy-like bud formation. *Ind. Crops Prod.* **2025**, *236*, 121995. [CrossRef]
9. Wu, G.; Pang, Y.; Tan, Y.; Peng, Z.; Geng, S.; Tao, G.; Li, Q.; Wang, S.; Zhang, L.; Tian, Q.; et al. An Efficient Plant Regeneration System for Different Explants of Rare and Endangered Plants in *Mussaenda anomala*. *Phyton* **2024**, *93*, 2597—-2611. [CrossRef]
10. Xue, W.; Liu, N.; Zhang, T.; Li, J.; Chen, P.; Yang, Y.; Chen, S. Substance metabolism, IAA and CTK signaling pathways regulating the origin of embryogenic callus during dedifferentiation and redifferentiation of cucumber cotyledon nodes. *Sci. Hortic.* **2022**, *293*, 110680. [CrossRef]
11. Sorokin, A.; Kovalchuk, I. Development of efficient and scalable regeneration tissue culture method for *Cannabis sativa*. *Plant Sci.* **2025**, *350*, 112296. [CrossRef]
12. Li, Y.; Jiang, H.; Qin, M.; He, Y.; Zhang, J.; Gong, W.; Xiao, X.; Li, P.; Zhou, W. Establishment of in vitro efficient regeneration system for leaves and hypocotyls of *Toona sinensis*, a multifunctional woody plants. *Ind. Crops Prod.* **2025**, *224*, 120328. [CrossRef]
13. Badhepuri, M.K.; Manokari, M.; Raj, M.C.; Jogam, P.; Dey, A.; Faisal, M.; Alatar, A.A.; Joshee, N.; Singisala, N.R.; Shekhawat, M.S. *Meta*-Topolin enhanced direct shoot organogenesis and regeneration from leaf explants of *Coleus forskohlii* (Willd.) Briq. *Ind. Crops Prod.* **2023**, *197*, 116584. [CrossRef]
14. Yang, X.; Li, Z.; Ma, J.; Chen, H.; He, J.; Liu, X.; Zhang, Y.; Liu, H.; Ye, D.; Tang, C. Efficient vegetative propagation and genetic transformation of Russian dandelion (*Taraxacum kok-saghyz* Rodin) from leaf explants. *Ind. Crops Prod.* **2024**, *209*, 118072. [CrossRef]
15. Wang, J.; Zhang, T.; Ren, L.; Nie, X.; Zhang, Z.; Wei, C.; Li, M.; Yan, X.; Huang, K.; Zhu, M.; et al. Establishment of a direct somatic embryogenesis regeneration system using immature cotyledon explants in *Camellia sinensis* cv. Shuchazao. *Ind. Crops Prod.* **2024**, *210*, 118076. [CrossRef]
16. Zhou, C.; Yang, M.; Luo, X.; Kuang, R.; Yang, H.; Yao, J.; Huang, B.; Wei, Y. Transcriptomic analysis of papaya (*Carica papaya* L.) shoot explants obtained by leaf- and stem-inoculation methods for adventitious roots induction. *Sci. Hortic.* **2021**, *276*, 109762. [CrossRef]
17. Hu, B.; Zhang, G.; Liu, W.; Shi, J.; Wang, H.; Qi, M.; Li, J.; Qin, P.; Ruan, Y.; Huang, H.; et al. Divergent regeneration-competent cells adopt a common mechanism for callus initiation in angiosperms. *Regeneration* **2017**, *4*, 132–139. [CrossRef]
18. Li, M.; Li, X.-T.; Zhang, X.-H.; Ai, J.; Shi, G.-L.; Wang, Z.-X.; Liang, L.-J.; Liu, J.-S.; Sun, D. Optimization of somatic embryogenesis system and accumulation of secondary metabolites in callus of *Schisandra chinensis* (Turcz.) Baill. *Ind. Crops Prod.* **2025**, *225*, 120572. [CrossRef]
19. Suwanseree, V.; Phansiri, S.; Yapwattanaphun, C. A comparison of callus induction in 4 Garcinia species. *Electron. J. Biotechnol.* **2019**, *40*, 45–51. [CrossRef]
20. Mazumdar, P.; Basu, A.; Paul, A.; Mahanta, C.; Sahoo, L. Age and orientation of the cotyledonary leaf explants determine the efficiency of de novo plant regeneration and Agrobacterium tumefaciens-mediated transformation in *Jatropha curcas* L. *S. Afr. J. Bot.* **2010**, *76*, 337–344. [CrossRef]
21. Hisano, H.; Matsuura, T.; Mori, I.C.; Yamane, M.; Sato, K. Endogenous hormone levels affect the regeneration ability of callus derived from different organs in barley. *Plant Physiol. Biochem.* **2016**, *99*, 66–72. [CrossRef]
22. Joshi, K.; Adhikari, P.; Jugran, A.; Bhatt, I.D. In vitro production of bioactive compounds and antioxidant potential in leaf-derived callus cultures of *Paeonia emodi* Royle. *Biochem. Syst. Ecol.* **2025**, *123*, 105101. [CrossRef]
23. Wiśniewska, J.; Kęsy, J.; Mucha, N.; Tyburski, J. Auxin resistant 1 gene (AUX1) mediates auxin effect on *Arabidopsis thaliana* callus growth by regulating its content and distribution pattern. *J. Plant Physiol.* **2024**, *293*, 154168. [CrossRef]
24. Abdouli, D.; Plačková, L.; Doležal, K.; Bettaieb, T.; Werbrouck, S.P.O. Topolin cytokinins enhanced shoot proliferation, reduced hyperhydricity and altered cytokinin metabolism in *Pistacia vera* L. seedling explants. *Plant Sci.* **2022**, *322*, 111360. [CrossRef]
25. Li, T.; Feng, Z.-Q.; Zhang, T.-T.; You, C.-X.; Zhou, C.; Wang, X.-F. The nitrate-responsive transcription factor *MdNLP7* regulates callus formation by modulating auxin response. *J. Integr. Agric.* **2023**, *22*, 3022–3033. [CrossRef]
26. Liu, J.; Gao, L.; Zhang, R.; Gao, A.; Oginga, Z.K.; Zheng, B.; Han, Y. ARF4 acting upstream of LBD16 promotes adventitious root formation in peach. *Hortic. Plant J.* **2025**, *11*, 145–161. [CrossRef]
27. Juárez-González, V.T.; Luján-Soto, E.; Aguirre de la Cruz, P.I.; Aquino-Luna, M.; Herrera-Díaz, J.; López-Ruiz, B.A.; Dinkova, T.D. Differential gene expression networks and auxin responses during maize callus induction from explant tissues with contrasting embryogenic potential. *J. Proteom.* **2025**, *318*, 105457. [CrossRef]
28. Khan, T.; Abbasi, B.H.; Zeb, A.; Ali, G.S. Carbohydrate-induced biomass accumulation and elicitation of secondary metabolites in callus cultures of *Fagonia indica*. *Ind. Crops Prod.* **2018**, *126*, 168–176. [CrossRef]

29. Kintzios, S.; Stavropoulou, E.; Skamneli, S. Accumulation of selected macronutrients and carbohydrates in melon tissue cultures: Association with pathways of in vitro dedifferentiation and differentiation (organogenesis, somatic embryogenesis). *Plant Sci.* **2004**, *167*, 655–664. [CrossRef]
30. Zahir, A.; Ahmad, W.; Nadeem, M.; Giglioli-Guivarc'h, N.; Hano, C.; Abbasi, B.H. In vitro cultures of *Linum usitatissimum* L.: Synergistic effects of mineral nutrients and photoperiod regimes on growth and biosynthesis of lignans and neolignans. *J. Photochem. Photobiol. B Biol.* **2018**, *187*, 141–150. [CrossRef] [PubMed]
31. Yang, Y.; Liu, C.; Yu, Y.; Ran, G.; Zhai, N.; Pi, L. *WUSCHEL RELATED HOMEOBOX5* and *7* maintain callus development by promoting cell division in Arabidopsis. *Plant Sci.* **2024**, *346*, 112133. [CrossRef]
32. Lu, X.; Fei, L.; Li, Y.; Du, J.; Ma, W.; Huang, H.; Wang, J. Effect of different plant growth regulators on callus and adventitious shoots induction, polysaccharides accumulation and antioxidant activity of *Rhodiola dumulosa*. *Chin. Herb. Med.* **2023**, *15*, 271–277. [CrossRef]
33. Iiyama, C.M.; Sartoratto, A.; Cardoso, J.C. Tissue-specific and novel secondary metabolites identified by SPME/GC-MS in *Artemisia annua* calli cultured under different wavelength. *Ind. Crops Prod.* **2024**, *208*, 117767. [CrossRef]
34. Liu, D.; Mu, Q.; Li, X.; Xu, S.; Li, Y.; Gu, T. The callus formation capacity of strawberry leaf explants is modulated by DNA methylation. *Hortic. Res.* **2022**, *9*, uhab073. [CrossRef]
35. Nunes, P.; Nunes, S.C.; Pereira, R.F.P.; Cruz, R.; Rocha, J.; Ravishankar, A.P.; Fernandes, L.; Bacelar, E.; Casal, S.; Anand, S.; et al. The leaf of *Agapanthus africanus* (L.) Hoffm.: A physical-chemical perspective of terrestrialization in the cuticle. *Environ. Exp. Bot.* **2023**, *208*, 105240. [CrossRef]
36. Gomaa, A.A.-R.; Younis, N.A.M.; Hofny, H.A.; Desoukey, S.Y.; Selim, A.H.I. Phytochemical characterization and biological evaluation of *Agapanthus africanus*: A combined experimental and in silico study. *S. Afr. J. Bot.* **2024**, *170*, 297–307. [CrossRef]
37. Younis, N.A.M.; Gomaa, A.A.; Ibrahim, A.H.; Abdelkader, M.S.A.; Desoukey, S.Y. The genus *Agapanthus*: A review of traditional uses, pharmacological and phytochemical attributes. *S. Afr. J. Bot.* **2022**, *150*, 1168–1183. [CrossRef]
38. Singh, D.N.; Verma, N.; Raghuwanshi, S.; Shukla, P.K.; Kulshreshtha, D.K. Antifungal activity of *Agapanthus africanus* extractives. *Fitoterapia* **2008**, *79*, 298–300. [CrossRef] [PubMed]
39. Yue, J.; Dong, Y.; Du, C.; Shi, Y.; Teng, Y. Transcriptomic and physiological analyses reveal the acquisition of somatic embryogenesis potential in *Agapanthus praecox*. *Sci. Hortic.* **2022**, *305*, 111362. [CrossRef]
40. Murashige, T.; Skoog, F. A Revised Medium for Rapid Growth and Bio Assays with Tobacco Tissue Cultures. *Physiol. Plant.* **1962**, *15*, 473–497. [CrossRef]
41. Chen, C.; Chen, H.; Zhang, Y.; Thomas, H.R.; Frank, M.H.; He, Y.; Xia, R. TBtools: An Integrative Toolkit Developed for Interactive Analyses of Big Biological Data. *Mol. Plant* **2020**, *13*, 1194–1202. [CrossRef] [PubMed]
42. Langfelder, P.; Horvath, S. WGCNA: An R package for weighted correlation network analysis. *BMC Bioinform.* **2008**, *9*, 559. [CrossRef]
43. Yue, J.-H.; Zhang, D.; Ren, L.; Shen, X.-H. Gibberellin and auxin signals control scape cell elongation and proliferation in *Agapanthus praecox* ssp. *orientalis*. *J. Plant Biol.* **2016**, *59*, 358–368. [CrossRef]
44. Livak, K.J.; Schmittgen, T.D. Analysis of relative gene expression data using real-time quantitative pcr and the $2^{-\Delta\Delta CT}$ method. *Methods* **2001**, *25*, 402–408. [CrossRef]
45. da Silva, J.A.T.; Gulyás, A.; Magyar-Tábori, K.; Wang, M.-R.; Wang, Q.-C.; Dobránszki, J. In vitro tissue culture of apple and other Malus species: Recent advances and applications. *Planta* **2019**, *249*, 975–1006. [CrossRef]
46. Mikuła, A.; Pożoga, M.; Grzyb, M.; Rybczyński, J.J. An unique system of somatic embryogenesis in the tree fern *Cyathea delgadii* Sternb.: The importance of explant type, and physical and chemical factors. *Plant Cell Tissue Organ Cult. (PCTOC)* **2015**, *123*, 467–478. [CrossRef]
47. Nurwahyuni, I.; Situmorang, M.; Sinaga, R. Plant Regeneration through Callus Cultures from Leaf Explant of Sumatra Benzoin (*Styrax benzoin*). *Int. J. For. Res.* **2020**, *2020*, 8860178. [CrossRef]
48. Mosoh, D.A.; Khandel, A.K.; Verma, S.K.; Vendrame, W.A. Effects of sterilization methods and plant growth regulators on in vitro regeneration and tuberization in *Gloriosa superba* (L.). *Vitr. Cell. Dev. Biol.-Plant* **2023**, *59*, 792–807. [CrossRef]
49. Huang, Y.; Huang, K.; Zhang, M.; Bu, W.; Yang, X.; Tian, J.; Lei, W. Study on adventitious root induction and endogenous hormone dynamics during cutting propagation of *Distylium chinense*. *Plant Sci.* **2025**, *355*, 112430. [CrossRef]
50. Suárez, E.; Alfayate, C.; Pérez-Francés, J.F.; Rodríguez-Pérez, J.A. Structural and ultrastructural variations in in vitro and ex vitro rooting of microcuttings from two micropropagated *Leucospermum* (Proteaceae). *Sci. Hortic.* **2018**, *239*, 300–307. [CrossRef]
51. Adem, M.; Sharma, L.; Shekhawat, G.S.; Šafranek, M.; Jásik, J. Auxin signaling, transport, and regulation during adventitious root formation. *Curr. Plant Biol.* **2024**, *40*, 100385. [CrossRef]
52. Kumar, V.; Moyo, M.; Gruz, J.; Šubrtová, M.; Van Staden, J. Phenolic acid profiles and antioxidant potential of *Pelargonium sidoides* callus cultures. *Ind. Crops Prod.* **2015**, *77*, 402–408. [CrossRef]
53. Liu, C.; Li, A.; Fan, X.; Qin, B.; Zhang, L. Explant browning during callus induction of *Juglans mandshurica* might be caused by the cooperation of PAL, polyphenol and PPO. *S. Afr. J. Bot.* **2024**, *174*, 937–945. [CrossRef]

54. Saranya, G.; Sruthi, D.; Jayakumar, K.S.; Jiby, M.V.; Nair, R.A.; Pillai, P.P.; Jayabaskaran, C. Polyphenol oxidase (PPO) arm of catecholamine pathway catalyzes the conversion of L-tyrosine to L-DOPA in *Mucuna pruriens* (L.) DC var. pruriens: An integrated pathway analysis using field grown and in vitro callus cultures. *Plant Physiol. Biochem.* **2021**, *166*, 1032–1043. [CrossRef]
55. Chang, E.; Guo, W.; Xie, Y.; Jiang, Z.; Dong, Y.; Jia, Z.; Zhao, X.; Liu, J.; Zhang, J. Changes of lignified-callus and wound-induced adventitious rooting in ancient *Platycladus orientalis* cuttings as affected by tree age. *Ind. Crops Prod.* **2023**, *203*, 117183. [CrossRef]
56. Zhang, Q.; Hu, H.; Huang, Y.; Han, K.; Xv, H.; Shen, Y.; Li, S.; Huang, J. The relationship between developmental stages of zygotic embryos at explanting and embryogenic frequency on hickory (*Carya cathayensis* Sarg.). *Sci. Hortic.* **2012**, *139*, 66–70. [CrossRef]
57. Wang, C.; Ma, H.; Zhu, W.; Zhang, J.; Zhao, X.; Li, X. Seedling-derived leaf and root tip as alternative explants for callus induction and plant regeneration in maize. *Physiol. Plant.* **2021**, *172*, 1570–1581. [CrossRef]
58. Hong, C.; Lee, H.G.; Shim, S.; Park, O.-S.; Kim, J.H.; Lee, K.; Oh, E.; Kim, J.; Jung, Y.J.; Seo, P.J. Histone modification-dependent production of peptide hormones facilitates acquisition of pluripotency during leaf-to-callus transition in Arabidopsis. *New Phytol.* **2024**, *242*, 1068–1083. [CrossRef]
59. Wu, L.-Y.; Shang, G.-D.; Wang, F.-X.; Gao, J.; Wan, M.-C.; Xu, Z.-G.; Wang, J.-W. Dynamic chromatin state profiling reveals regulatory roles of auxin and cytokinin in shoot regeneration. *Dev. Cell* **2022**, *57*, 526–542.e527. [CrossRef]
60. Apostolou, E.; Hochedlinger, K. Chromatin dynamics during cellular reprogramming. *Nature* **2013**, *502*, 462–471. [CrossRef]
61. Arabia, A.; Munné-Bosch, S.; Muñoz, P. Ascorbic acid as a master redox regulator of fruit ripening. *Postharvest Biol. Technol.* **2024**, *207*, 112614. [CrossRef]
62. Su, Y.H.; Tang, L.P.; Zhao, X.Y.; Zhang, X.S. Plant cell totipotency: Insights into cellular reprogramming. *J. Integr. Plant Biol.* **2021**, *63*, 228–243. [CrossRef] [PubMed]
63. Wang, W.; Zhang, C.; Guo, H.; Chen, F. A novel auxin methyltransferase of the SABATH family for phenylacetic acid methylation is conserved in potato and tomato. *Plant Physiol. Biochem.* **2025**, *224*, 109972. [CrossRef]
64. Zeng, W.; Li, J.; Li, D.; Lu, J.; Pan, Y.; Wei, H.; Chen, Y.; Shu, Q.; Bian, H.; Guo, F. Interaction between OsLEC1 and OsHDA710 positively regulates callus formation in rice. *Plant Physiol. Biochem.* **2025**, *223*, 109826. [CrossRef] [PubMed]
65. Wang, Y.; Sun, X.; Peng, J.; Li, F.; Ali, F.; Wang, Z. Regulation of seed germination: ROS, epigenetic, and hormonal aspects. *J. Adv. Res.* **2025**, *71*, 107–125. [CrossRef]
66. Zhai, N.; Pan, X.; Zeng, M.; Xu, L. Developmental trajectory of pluripotent stem cell establishment in Arabidopsis callus guided by a quiescent center-related gene network. *Development* **2023**, *150*, dev200879. [CrossRef]
67. Nhut, D.T.; Khai, H.D.; Hung, N.V.; Vinh, N.Q.; Dung, D.M.; Tung, H.T.; Mai, N.T.N.; Luan, V.Q.; Cuong, D.M. Effect of explant age on phytochemicals and morphogenesis in begonia. *Plant Cell Tissue Organ Cult. (PCTOC)* **2023**, *155*, 267–282. [CrossRef]
68. Yang, C.; Ying, S.; Tang, B.; Yu, C.; Wang, Y.; Wu, M.; Liu, M. The mechanistic insights into fruit ripening: Integrating phytohormones, transcription factors, and epigenetic modification. *J. Genet. Genom.* **2025**, *52*, 1475–1489. [CrossRef]
69. Wang, S.; Li, F.; Wang, G.; Li, H.; Li, X.; Cao, X.; Wang, J. Polyphenol oxidase gene editing changed the flavonoid composition and browning process of litchi (*Litchi chinensis* Sonn.) callus. *Gene* **2025**, *936*, 149130. [CrossRef]
70. Wang, Y.; Ye, H.; Lin, W.; Wang, G.; Luo, T.; He, J.; Wang, B. Cinnamic acid application inhibits the browning of cold-stored taro slices by maintaining membrane function, reducing flavonoid biosynthesis and enhancing glutathione metabolism. *Postharvest Biol. Technol.* **2024**, *218*, 113180. [CrossRef]
71. Peer, W.A.; Murphy, A.S. Flavonoids and auxin transport: Modulators or regulators? *Trends Plant Sci.* **2007**, *12*, 556–563. [CrossRef] [PubMed]
72. Jiang, S.; Zhang, S.; Li, P.; Xue, N.; Chen, K.; Ji, X.; Ji, W. Response of dauciform roots to low phosphorus stress: Insights based on ecophysiology, transcriptomics, and metabolomics analysis. *Ind. Crops Prod.* **2025**, *234*, 121563. [CrossRef]
73. Delannoy, E.; Batardiere, B.; Pateyron, S.; Soubigou-Taconnat, L.; Chiquet, J.; Colcombet, J.; Lang, J. Cell specialization and coordination in Arabidopsis leaves upon pathogenic attack revealed by scRNA-seq. *Plant Commun.* **2023**, *4*, 100676. [CrossRef] [PubMed]

Disclaimer/Publisher's Note: The statements, opinions and data contained in all publications are solely those of the individual author(s) and contributor(s) and not of MDPI and/or the editor(s). MDPI and/or the editor(s) disclaim responsibility for any injury to people or property resulting from any ideas, methods, instructions or products referred to in the content.